

Generation and Breakup of Worthington Jets After Cavity Collapse.

STEPHAN GEKLE¹ AND J. M. GORDILLO²

¹ Department of Applied Physics and J.M. Burgers Centre for Fluid Dynamics, University of Twente, P.O. Box 217, 7500 AE Enschede, The Netherlands

² Área de Mecánica de Fluidos, Departamento de Ingeniería Aeroespacial y Mecánica de Fluidos, Universidad de Sevilla, Avda. de los Descubrimientos s/n 41092, Sevilla, Spain.

(Received ?? and in revised form ??)

Helped by the careful analysis of their experimental data, Worthington & Cole (1897, 1900) described roughly the mechanism underlying the formation of high-speed jets ejected after the impact of an axisymmetric solid on a liquid-air interface. They made the fundamental observation that the intensity of these sharp jets was intimately related to the formation of an axisymmetric air cavity in the wake of the impactor. In this work we combine detailed boundary-integral simulations with analytical modeling to describe the formation and break-up of such Worthington jets in two common physical systems: the impact of a circular disc on a liquid surface and the release of air bubbles from an underwater nozzle. We first show that the jet base dynamics can be predicted for both systems using our earlier model in Gekle, Gordillo, van der Meer and Lohse. *Phys. Rev. Lett.* 102 (2009). Nevertheless, our main point here is to present a model which allows us to accurately predict the shape of the entire jet. In our model, the flow structure inside the jet is divided into three different regions: The *axial acceleration region*, where the radial momentum of the incoming liquid is converted into axial momentum, the *ballistic region*, where fluid particles experience no further acceleration and move constantly with the velocity obtained at the end of the acceleration region and the *jet tip region* where the jet eventually breaks into droplets. Good agreement with numerics and some experimental data is found. Moreover, we find that, contrarily to the capillary breakup of liquid cylinders in vacuum studied by Rayleigh (1878), the breakup of stretched liquid jets at high values of both Weber and Reynolds numbers is not triggered by the growth of perturbations coming from an external source of noise. Instead, the jet breaks up due to the capillary deceleration of the liquid at the tip which produces a corrugation to the jet shape. This perturbation, which is self-induced by the flow, will grow in time promoted by a capillary mechanism. Combining these three regions for the base, the jet, and the tip we are able to predict the exact shape evolution of Worthington jets ejected after the impact of a solid object - including the size of small droplets ejected from the tip due to a surface-tension driven instability - using as the single input parameters the minimum radius of the cavity and the flow field *before* the jet emerges.

1. Introduction

The impact of a solid object against a liquid interface is frequently accompanied by the ejection of a high speed jet emerging out of the liquid bulk into the air. Figure 1, which shows the effect of a horizontal disc that impacts on a pool of water, illustrates a liquid

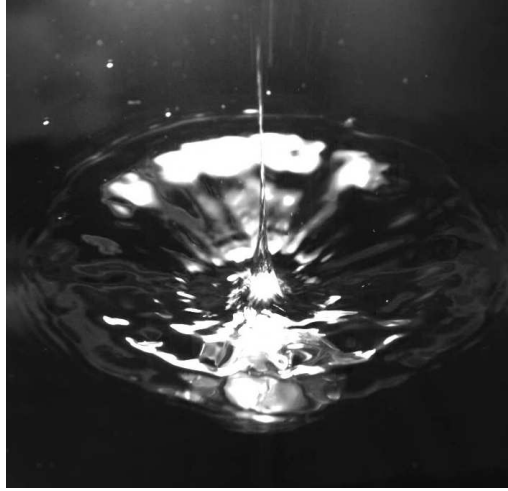


FIGURE 1. Image of the high-speed jet ejected after the impact of 2cm disc with 1 m/s on a quiescent water surface.

jet which flows ~ 20 times faster than the disc impact speed. The qualitative description of this common and striking phenomenon was firstly elucidated at the beginning of the twentieth century by Worthington & Cole (1897, 1900). Through the careful analysis of the photographs taken after a solid sphere was dropped into water, Worthington & Cole (1897, 1900) realized that these type of liquid threads emerge as a consequence of the hydrostatic collapse of the air-filled cavity which is created at the wake of the impacting solid. Worthington & Cole (1897, 1900) also made the remarkable observation that the generation of such cavities was very much influenced by the surface properties of the spherical solid. One century after their original observations, Duez *et al.* (2007) quantified the conditions that determine the existence of the air cavity in terms of the surface properties of the solid and the material properties of the liquid.

High speed jets emerging out of a liquid interface are also frequently observed in many other situations. For instance, it is very usual to perceive that the liquid “jumps” out of the surface of sparkling drinks, a fact which is known to happen as a consequence of bubbles bursting at the liquid interface [Boulton-Stone & Blake (1993); Duchemin *et al.* (2002); Liger-Belair *et al.* (2008)]. Similarly, the impact of a drop on a liquid interface or solid surface [Oguz & Prosperetti (1990); Shin & McMahon (1990); Rein (1993); Morton *et al.* (2000); Deng *et al.* (2007); Bartolo *et al.* (2006)], is commonly accompanied by the ejection of liquid jets whose velocities can be substantially larger than that of the impacting drop. Less familiar situations such as those related to the focussing of capillary [MacIntyre (1968); Thoroddsen *et al.* (2007*b*)] or Faraday waves [Hogrefe *et al.* (1998); Zeff *et al.* (2000)] also give rise to the same type of phenomenon. Nevertheless, in spite of the clear analogies, the main difference between the situations enumerated above and the case of jet formation after cavity collapse is that, in the latter case, surface tension does not play any role in the jet ejection process [see Gekle, Gordillo, van der Meer & Lohse (2009*a*) for details]. Indeed, the type of Worthington jets to be described here depend on a purely inertial mechanism, namely the radial energy focussing along the narrow cavity wall right before the cavity pinches-off. This fact makes our process also somewhat different from situations in which jets are induced by pressure waves [Ohl & Ikink (2003); Tjan & Phillips (2007); Antkowiak *et al.* (2007); Blake *et al.* (1993)].

Moreover, contrarily to what could be expected from the analogy with other related physical situations [Longuet-Higgins (1983); Longuet-Higgins & Oguz (1995)], Gekle *et al.* (2009a) pointed out that jets formed after cavity collapse are not significantly influenced by the hyperbolic type of flow existing at the pinch-off location. Instead, the description of this type of jets shares many similarities with the very violent jets of fluidized metal which are ejected after the explosion of lined cavities [e.g. Birkhoff *et al.* (1948)], with those formed when an axisymmetric bubble collapses inside a stagnant liquid pool [Manasseh *et al.* (1998); Bolanos-Jiménez *et al.* (2008)] or possibly even with the granular jets observed when an object impacts a fluidized granular material [Thoroddsen & Shen (2001); Lohse *et al.* (2004)].

Most of the results presented here refer to the perpendicular impact of a circular disc with radius R_D and constant velocity V_D against a liquid surface. The fact that the solid is a disc instead of a sphere leads to the formation of an air cavity which is attached at the disc periphery, independent of the surface properties. Thus, this choice for the solid geometry avoids the additional difficulty of determining the position of the void attachment line on the solid surface. The differences pointed out above set our system somewhat apart from similar studies [Duclaux *et al.* (2007); Glasheen & McMahon (1996)]. The experimental realization of the setup to which the numerical simulations presented are referred, is described by Bergmann *et al.* (2006, 2009); Gekle *et al.* (2008, 2009a), who show that boundary-integral simulations are in excellent agreement with experiments. In addition, potential flow numerical simulations to study of the type of Worthington jets ejected after bubble pinch-off from an underwater nozzle sticking into a quiescent pool of water [Manasseh *et al.* (1998); Longuet-Higgins *et al.* (1991); Oguz & Prosperetti (1993); Burton *et al.* (2005); Keim *et al.* (2006); Thoroddsen *et al.* (2007a, 2008); Gordillo *et al.* (2007); Burton & Taborek (2008); Gordillo (2008); Bolanos-Jiménez *et al.* (2008); Schmidt *et al.* (2009)] are also reported in this paper. As in the case of Worthington jets ejected after solid body impact, similar boundary-integral simulations have been shown to be in excellent agreement with experiments [see Oguz & Prosperetti (1993); Bolanos-Jiménez *et al.* (2008)].

This paper is organized as follows: In section 2 we present the three different numerical methods used. Section 3 presents the results from the simulations which are compared to the analytical model in section 4. Conclusions are drawn in section 5.

2. Numerical methods

In this paper we have used three types of boundary-integral simulations. The first two model, respectively, the normal impact of a disc on a free surface and the pinch-off of a bubble from an underwater nozzle. With the purpose of simulating the capillary breakup of the jets formed in the first two situations, the third type of simulation represents a jet issued from a constant-diameter nozzle with an imposed axial strain rate. The latter type of numerical simulations have the advantage of allowing us to directly impose the values of both the strain rate and the Weber number, which are the parameters controlling the breakup of the jet, as will become clear from the discussion below.

2.1. Disc impact simulations

The process of disc impact [see also Bergmann *et al.* (2006, 2009); Gekle *et al.* (2009a)] is illustrated in figure 2: after impact a large cavity is created beneath the surface which subsequently collapses about halfway due to the hydrostatic pressure from the liquid bulk. From the closure location two high-speed jets are ejected up- and downwards. Here positions, velocities and time are made dimensionless using as characteristic quantities

the disc radius R_D , the impact velocity V_D , and $T_D = R_D/V_D$, respectively. (Variables in capital letters will be used to denote dimensional quantities whereas their lower case analogs will indicate the corresponding dimensionless variable). Moreover, it will be assumed that axisymmetry is preserved and, thus, a polar coordinate system (r, z) will be used. The origins of both the axial polar coordinate z and of time t are set at the cavity pinch-off height and at the pinch-off instant, respectively.

Since global and local Reynolds numbers are large and the generation of vorticity is negligible [Bergmann *et al.* (2009); Gekle *et al.* (2009a)] we can make use of a flow potential to describe the liquid flow field. The numerical details, including the “surface surgery” needed to accurately capture the transition from the cavity collapse process to the jet ejection, are given elsewhere [see Gekle *et al.* (2009a); Bergmann *et al.* (2009)]. These simulations have shown excellent agreement with experimental high-speed recordings and particle image velocimetry measurements [Bergmann *et al.* (2006); Gekle *et al.* (2008, 2009a); Bergmann *et al.* (2009)]. The simulation stops when the downward jet hits the disc surface.

Since the Reynolds number is large, the dimensionless parameters controlling the jet ejection process are the Froude number, $\text{Fr} = V_D^2/(R_D g)$, and the Weber number, $\text{We} = \rho V_D^2 R_D/\sigma$ where g , ρ and σ indicate the gravitational acceleration, the liquid density and the interfacial tension, respectively. Since $\text{We} \gtrsim O(10^2)$ in all cases considered here, the jet ejection is not promoted by surface tension [Gekle *et al.* (2009a)]. Nonetheless, capillarity is essential to describe the jet breakup process, as will become clear from the discussion below. Air effects, which play an essential role during the latest stages of cavity collapse [Gordillo, Sevilla, Rodríguez-Rodríguez & Martínez-Bazán (2005); Gordillo (2008); Gekle, Peters, Gordillo, van der Meer & Lohse (2009b)], are not taken into explicit consideration here. Instead the cut-off radius at which the cavity geometry is changed into the jet geometry is fixed manually verifying carefully that the exact value of this parameter does not influence our results. The only consequence of this simplification is that a tiny fraction of the jet - the jet tip - may not be accurately described neither by our numerical simulations nor by our theory as will be discussed in section 3.1.

2.2. Bubble pinch-off from an underwater nozzle

In the second type of simulations a bubble grows and detaches when a constant gas flow rate is injected from an underwater nozzle into a quiescent pool of liquid. Manasseh *et al.* (1998) and Bolanos-Jiménez *et al.* (2008) experimentally showed that this process also creates high speed jets. Indeed, as the bubble grows in size, the neck becomes more and more elongated and, eventually, surface tension triggers the pinch-off of the bubble, leading to the formation of two fast and small jets as illustrated in figure 3. Surface tension also leads to the pinch-off of a small droplet at the jet tip, which is precisely the instant when the simulation stops.

Here, distances are made non-dimensional using the nozzle radius R_N as the characteristic length scale; moreover, the prescribed gas flow rate Q is used to derive the typical time scale $T_N = (\pi R_N^3)/Q$. For the quasi-static injection conditions considered here, the relevant dimensionless parameter characterizing this physical situation is the Bond number $\text{Bo} = \rho R_N^2 g/\sigma$ [Longuet-Higgins *et al.* (1991); Bolanos-Jiménez *et al.* (2008)], which in the case presented here equals 2.1. More details of our simulation method are given in Oguz & Prosperetti (1993); Gekle *et al.* (2009c). Note that the present numerical simulations [Oguz & Prosperetti (1993)] as well as those reported using a very similar numerical method [Bolanos-Jiménez *et al.* (2008)], are in excellent agreement with experiments.

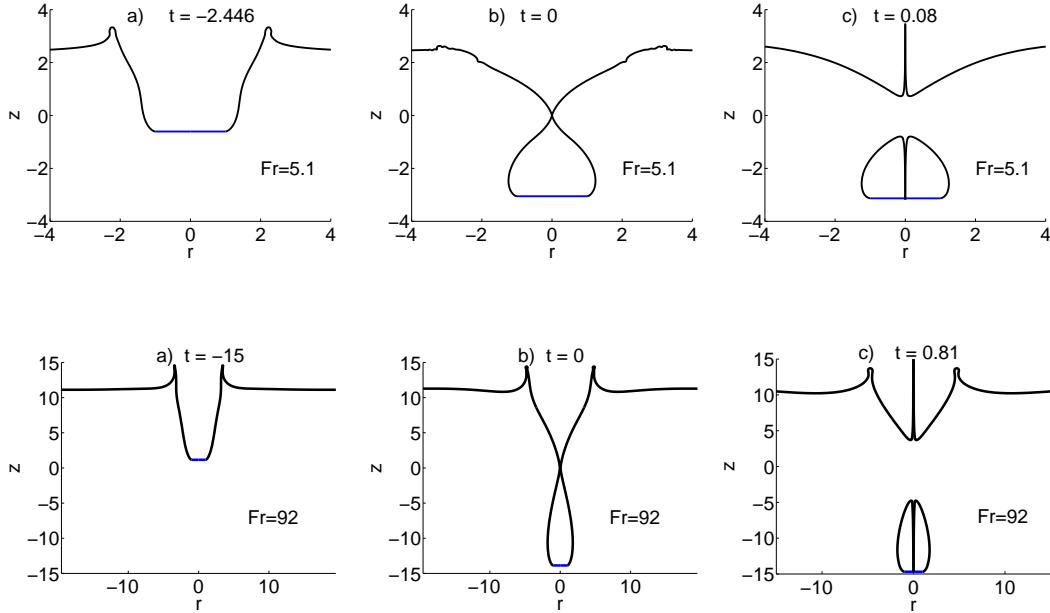


FIGURE 2. Numerical results obtained when a circular disc (blue line) impacts perpendicularly and at constant velocity on a flat liquid interface. Upon impact a cavity attached at the disc periphery is created in the liquid (a) which collapses under the influence of hydrostatic pressure (b). As a consequence of the cavity collapse, two jets with velocities much larger than that of the impact solid, are ejected upwards and downwards. The influence of increasing the impact Froude number from $Fr = 5.1$ – top row – to $Fr = 92$ – bottom row – is that the cavity becomes more slender.

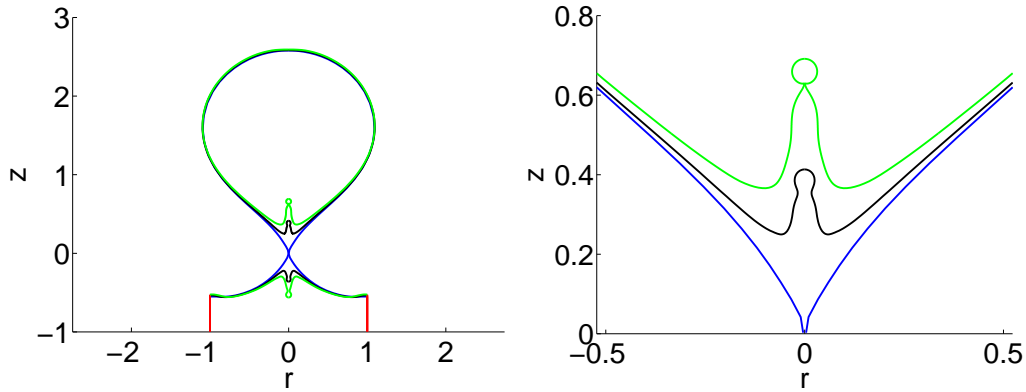


FIGURE 3. (a) Time evolution of jets formed after the collapse of gas bubbles injected into a quiescent liquid pool through a nozzle (red line), showing the ejection of the first drop, for $Bo = 2.1$. (b) Closeup view of the jet region in (a). The colors correspond to different dimensionless times: $t = 0$ (blue), $t = 0.0014$ (black) and $t = 0.0027$ (green)

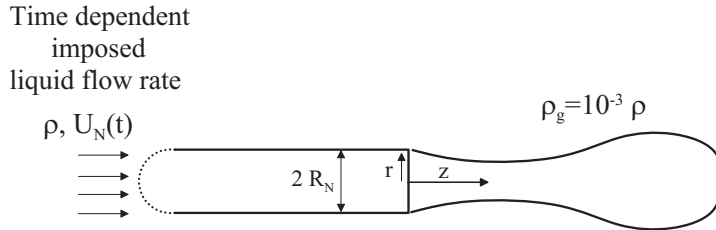


FIGURE 4. Sketch defining the geometry of the numerical simulations used to describe the capillary breakup of a stretched liquid jet of density ρ injected into a gaseous atmosphere of density $\rho_g = 10^{-3}\rho$. The liquid velocity profile imposed at the boundary which delimits the nozzle on the left is uniform and decreases linearly with time.

2.3. Simulations of a jet ejected at constant diameter

As will be shown by our theoretical analysis below, the jet breakup process can be described in terms of two dimensionless parameters evaluated nearby the base of the jet, namely, the local Weber number and the dimensionless axial strain rate. These quantities depend non-trivially on the input parameters of our physical simulations (disc speed, nozzle size etc.). In order to obtain a way of systematically varying both the local Weber number and strain rate we conducted a third type of simulation by adapting the axisymmetric (two-fluid) boundary integral method described in Gordillo *et al.* (2007) to a situation that retains the essential ingredients to describe the capillary breakup process in the first two types of simulations. For this purpose, we have simulated the discharge of a liquid injected through a constant radius needle with a length of 20 times its radius into a gaseous atmosphere. The density ratio of the inner and outer fluids is 10^3 and a uniform velocity profile linearly decreasing with time is imposed on the boundary that delimits the computational domain on the left (see figure 4). Initially, the liquid interface is assumed to be a hemisphere attached at the nozzle tip. The uniform velocity with which the liquid is injected varies in time according to

$$U_N(t_N) = U_N(0)(1 - \alpha t_N) \quad (2.1)$$

with the dimensionless strain rate α and the initial velocity $U_N(0)$ determined by the physical situation which one intends to imitate (jets formed either after the disc impact or from the underwater nozzle). For these type of simulations positions, velocities and time will be made non dimensional using, as characteristic dimensional quantities, the injection needle radius R_N , the initial velocity $U_N(0)$, and $T_N = R_N/U_N(0)$ respectively.

In section 3.4 we demonstrate very good agreement between the results of these type of simulations and those related to the formation of jets after bubble pinch-off from an underwater nozzle. Unfortunately, the extremely large values of the Weber number reached at the tip of the liquid jets formed after the impact of a disc on a free surface ($\sim O(10^3)$) unavoidably lead to the development of numerical instabilities [Tjan & Phillips (2007)]. This fact makes a direct comparison between the simulations of the axial strain system sketched in figure 4 and those corresponding to the impacting disc impossible.

3. Analysis of numerical results

3.1. Effects of azimuthal asymmetries in the determination of the cut-off radius

The value of r_{min} (the minimum radius of the cavity before the jet emerges) would be zero under the ideal conditions of our simulations, which do not take into account gas effects

[Gordillo *et al.* (2005); Gordillo (2008); Gekle *et al.* (2009b); Burton & Taborek (2008)], liquid viscosity [Burton *et al.* (2005); Thoroddsen *et al.* (2007a); Bolanos-Jiménez *et al.* (2009)] or small azimuthal asymmetries that may be present in the flow [Keim *et al.* (2006); Schmidt *et al.* (2009)]. This would imply that the initial jet velocity would be infinity. However, all the effects enumerated above are known to strongly influence the spatial region surrounding the cavity neck during the very last stages of bubble pinch-off and, therefore, are essential to determine the real value of r_{min} (Gordillo (2008); Gekle *et al.* (2009b)).

Note first that, the larger r_{min} is, the smaller will be the maximum liquid velocity at the tip of the jet. Here we will provide experimental evidence showing that non-axisymmetric perturbations are of crucial importance to fix r_{min} and, consequently, the maximum velocity reached by the jet. This is due to the fact that asymmetries influence the radial flow focussing effect on the central axis even before the actual cavity closure. The development of azimuthal instabilities leads to a decrease of the liquid acceleration towards the axis before pinch-off and thus reduces the speed of the ejected jet. This is clearly observed in figures 5 and 6, which show the cavity formation and jet ejection processes when either a brass disc (smooth surface) or a golf ball (structured surface) impact perpendicularly on a quiescent pool of water. Despite the fact that both the velocity and the diameter of the ball are larger than those of the disc, the maximum jet velocity is larger for the disc case. Indeed, while the shape of the cavity in figure 5 is smooth, the cavity interface in figure 6 clearly exhibits asymmetric modulations already right after the impact (which – in addition to the rough surface structure – may in part also be due to a rotation of the ball). Note that the overall shape of the cavity is very similar in both cases. Consequently, since the self-acceleration of the liquid towards the axis is lost when the amplitude of azimuthal disturbances is similar to the radius of the cavity, the maximum velocity reached during the collapse process decreases when the cavity interface is not smooth. Note that figures 5 and 6 are representative of an exhaustive set of experiments. The analysis of the whole experimental data has shown that the rough surface systematically produces lower jet speeds.

The initial amplitude or the precise instant at which such azimuthal instabilities may develop is not easy to predict. For instance, Keim *et al.* (2006); Schmidt *et al.* (2009) pointed out that tiny geometrical asymmetries in the initial setup might break the cylindrical symmetry of the cavity at the pinch-off location. Moreover, even if the cavity is perfectly axisymmetric, the strong shear between the gas and the liquid will induce instabilities that tend to break the cylindrical symmetry of the cavity [Leppinen & Lister (2003); Bergmann *et al.* (2006)].

Therefore, the precise determination of r_{min} is a very complex and difficult subject which in addition will heavily depend on the system under study and must therefore remain outside the scope of this contribution. We have instead decided to vary r_{min} within reasonable bounds and to analyze carefully the effect on the subsequent time evolution of the jet. It can be clearly appreciated in figure 7 that differences in the simulations can be observed in both the jet base and tip region right after pinch-off occurs. However, as soon as the jet radius at its base becomes of the order of the maximum value of r_{min} explored, differences in the jet base region disappear and only remain appreciable in the jet tip region. Physically, this means that gas effects and small asymmetries will only be felt at the highest part of the jet, which represents only a very small fraction of both the total volume and of the total kinetic energy of the jet. Note also that, in spite of the jet tip being the spatial region where the highest velocities are reached, it is also the least reproducible one from an experimental point of view since it strongly depends on the precise details of pinch-off. Thus, regarding experimental reproducibility, our study

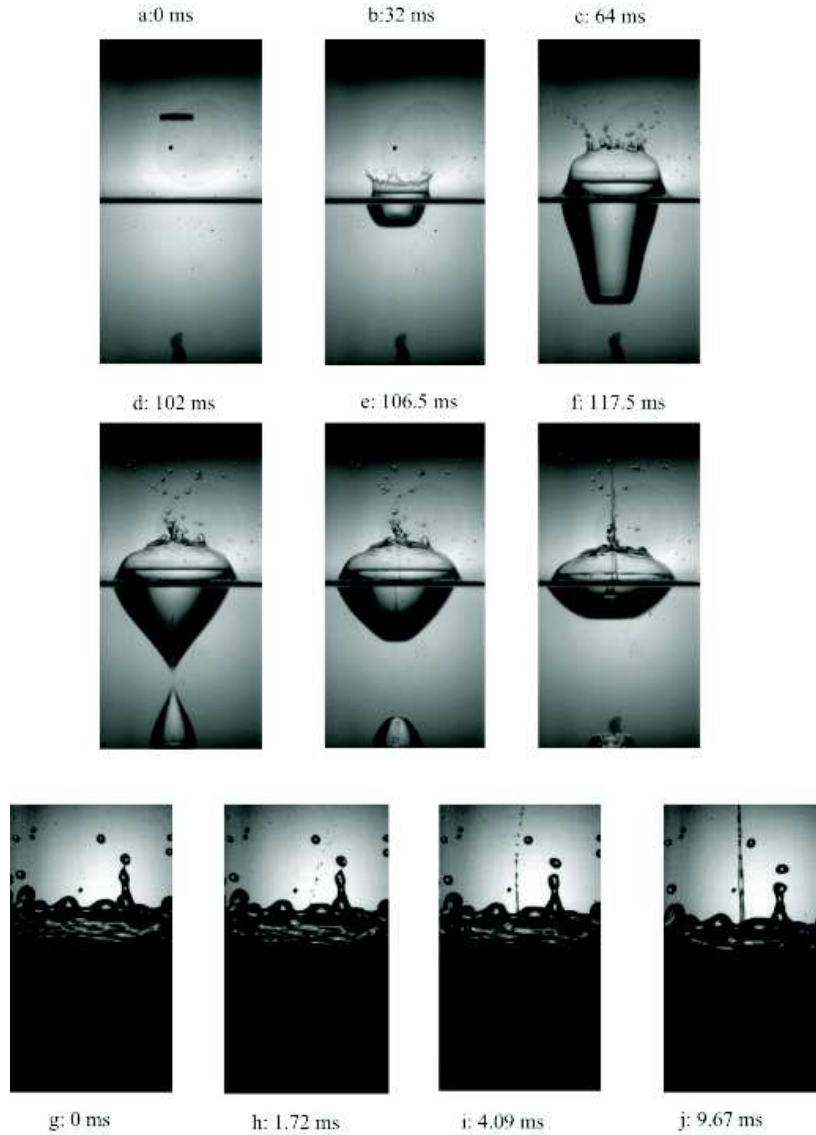


FIGURE 5. Pictures (a)-(f) show the smooth cavity formed after the normal impact of a brass disc against a water interface. The disc dimensions are 22 mm in diameter and 4.7 mm in height. The disc falls by gravity and the impact velocity is $V_{\text{impact}} = 1.85$ m/s. Note that, while the time between impact and cavity closure is roughly 70 ms, the upwards jet reaches the free surface in less than 4 ms, indicating that the jet velocity is much larger than the impactor's velocity. Indeed, the initial velocity of the tip of the jet, measured from detailed images of the type (g)-(j), is larger than – since drops might not be in a plane perpendicular to the free surface – 22.71 m/s and thus larger than 12.28 times the disc velocity. The huge velocities reached by the liquid jet can also be visually appreciated by comparison with the velocity of the drops formed in the corona splash which hardly change their position between images (g) and (j). Let us also remark that, initially, the jet is not axisymmetric ((h) and (i)). Nevertheless, after a few milliseconds, picture (j) shows that the jet becomes approximately axisymmetric.

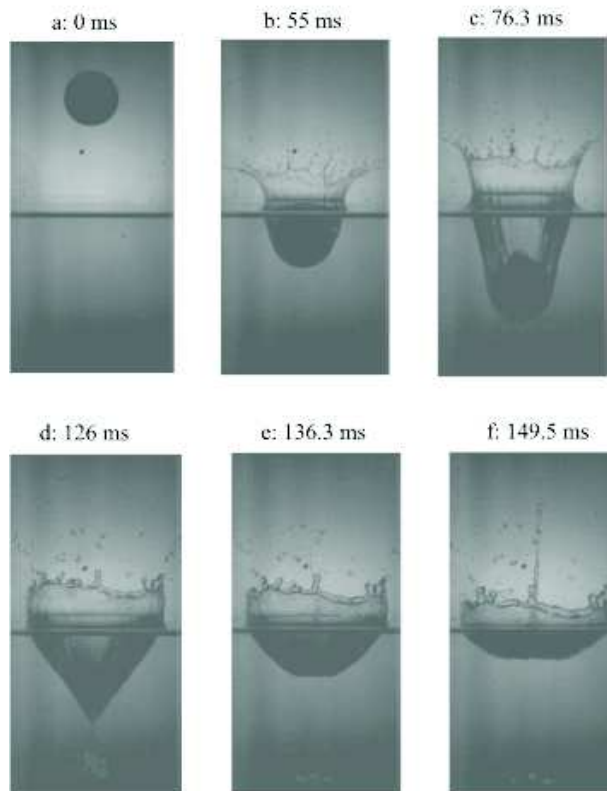


FIGURE 6. Pictures (a)-(f) show the cavity formation caused by a golf ball with a diameter of 42.75 mm impacting with a velocity of 2.03 m/s. Compared to figure 5 the surface shape is visibly distorted (c) due to the rough surface structure of the ball. Nevertheless, it can be inferred from a detailed image analysis that the jet velocity is again much larger than the ball's velocity. However, in spite of both the impact velocity and the ball diameter being larger than those of the disc, the maximum velocity of the jet is only $V_{\text{impact}} \simeq 20$ m/s and thus smaller than for the impacting disc.

will be valid to accurately describe the most robust part of the jet. In the case of the impacting disc we will set $r_{\text{min}} = 0.01$ and in the case of the gas injection needle, the minimum radius will be fixed to $r_{\text{min}} = 0.05$.

Finally, note that our axisymmetric approach has been proven to be in excellent agreement with experiments whenever either the radius of the collapsing cavity or the radius of the emerging jet, are larger than the cut-off radius r_{min} for which any of the effects enumerated above – gas, azimuthal perturbations – become relevant [see, for instance, Bergmann *et al.* (2006); Gekle *et al.* (2008); Bolanos-Jiménez *et al.* (2008); Gekle *et al.* (2009a); Bolanos-Jiménez *et al.* (2009)].

3.2. Jet ejection process for the disc impact

The different stages of the jet formation process have been illustrated in figure 2. After the solid body impacts against the free surface, an air cavity is generated (a). As a consequence of the favorable pressure gradient existing from the bulk of the liquid to the cavity interface, the liquid is accelerated inwards (b). These radially inward velocities focus the liquid towards the axis of symmetry, leading to the formation of two fast and sharp fluid jets shooting up- and downwards, as depicted in figure 2 (c). Here we will

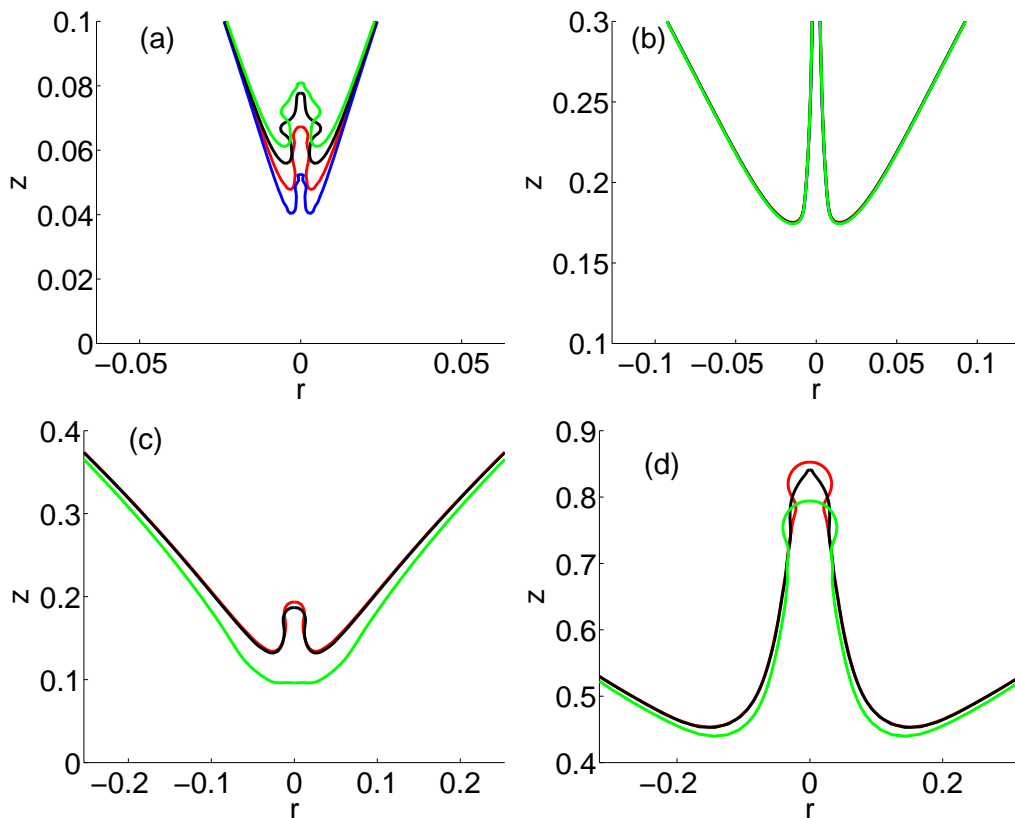


FIGURE 7. Top row: Jet shapes for the disc impact at $Fr=5.1$ at two different instants of time, $t=10^{-4}$ (a) and $t=3.2 \times 10^{-3}$ (b), for four different values of the cut-off radius, $r_{min}=0.005$ (blue), $r_{min}=0.01$ (red), $r_{min}=0.02$ (black), and $r_{min}=0.05$ (green). Bottom row: Jet shapes for the underwater nozzle with different cut-off radii (colors as in top row) at $t=0.0003$ (c) and $t=0.004$ (d), respectively (here the simulations are extended beyond the ejection of the first droplet). It is evident in both cases that the influence of varying the cut-off is significant only in the very first instants after pinch-off and at the very tip of the jet.

mainly focus on the detailed description of the upwards jet and demonstrate that the downward jet can be treated in the same way.

From figure 2, observe that larger Froude numbers create more slender cavities and also increase the non-dimensional depth at which the cavity pinches-off. Furthermore, it can be appreciated that the jets are extremely thin and that the time needed for the tip of the jet to reach the free surface is only a small fraction of the pinch-off time. This latter observation means that the jets possess a much faster velocity than the velocity of the impacting solid, a conclusion which was also extracted from the analysis of the experiments in figures 5-6. Motivated by this striking fact, one of the main objectives in this paper will be to address the following question: what is the relationship between the impact velocity V_D - or, in dimensionless terms, between the Froude number - and the liquid velocity within the jet?

With this purpose in mind, it will prove convenient to define first the length scale that characterizes the jet width. In Gekle *et al.* (2009a) we showed that the time evolution of the jet is a *local* phenomenon, independent of the stagnation-point type of flow generated

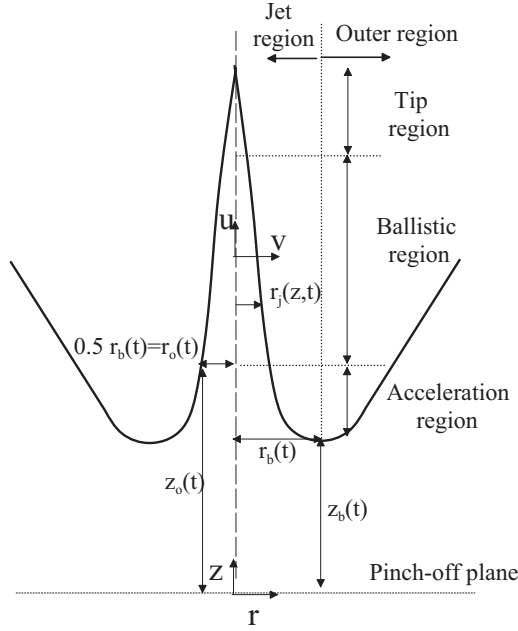


FIGURE 8. Sketch showing the different lengths used to define the jet base and the regions of the jet. The jet base (r_b, z_b) is located where the interface possesses a local minimum. The outer region covers the bulk of the fluid with $r > r_b$ and $z < z_b$. The jet region is subdivided into the acceleration, the ballistic and the tip region. Note that, in the following, u and v will be used to denote axial and radial velocities, respectively

after pinch-off at the location where the cavity collapses. Therefore, this characteristic length needs to be related to a *local* instead of a global quantity and, following Gekle *et al.* (2009a), we choose the radial position at which the interface possesses a local minimum i.e., the radius $r_b(t)$ indicated in figure 8. We shall in the following call this point the *jet base* and denote its vertical position by $z_b(t)$.

To clearly show the spatial region surrounding the jet base, some of the different jet shapes taken from the time evolutions of figure 2, are translated vertically so that they share a common vertical origin, as depicted in figure 9. Note that both the jet base and the jet itself widen as the time from pinch-off increases. Interestingly enough, figure 10 shows that jet shapes exhibit some degree of self-similarity since they nearly collapse onto the same curve when distances are normalized using r_b . This fact indicates that r_b is not an arbitrary choice, but a relevant local length that plays a key role in the dynamics of the jet. The same arguments hold for the downward jet as illustrated in figure 11.

In order to model the full process of jet ejection and break-up we divide the liquid flow field into two different regions: the outer region, defined for $r > r_b$, $z < z_b$ and the jet region, extending from the jet base to the axis i.e., $r < r_b$ and $z \geq z_b$, as illustrated in figure 10. The jet region is further divided into three different axial subregions: the *acceleration region*, the *ballistic region* and the *tip region* as illustrated in figure 8.

Figure 12 shows that $z_b(t) \gg r_b(t)$. These comparatively large values of $z_b(t)$ with respect to $r_b(t)$ are caused by the confinement of the jet by the cavity walls, which inhibits the widening of the base radius. Moreover, the small values of r_b are responsible for the large axial velocities within the jet (and, thus, for the large values of dz_b/dt) since, as it will become clear below, vertical velocities are inversely proportional to r_b .

The importance of local processes around the jet base is even more clearly illustrated

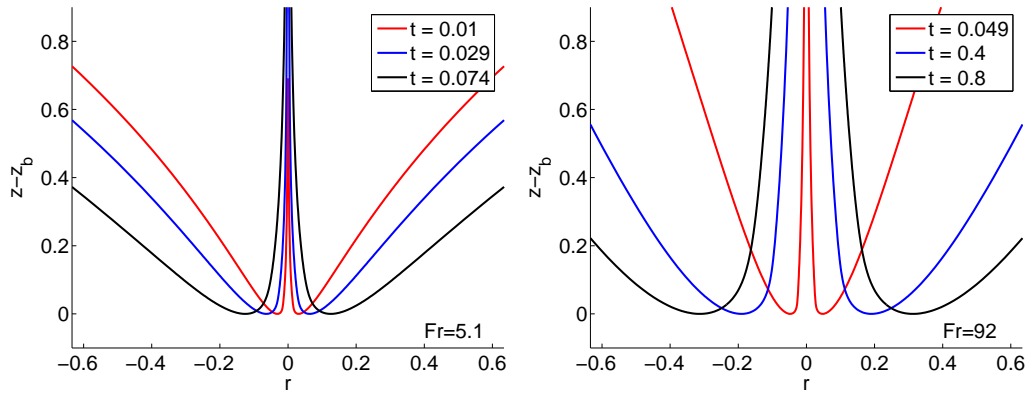


FIGURE 9. Jet shapes translated vertically for different instants of time and different values of the impact Froude number.

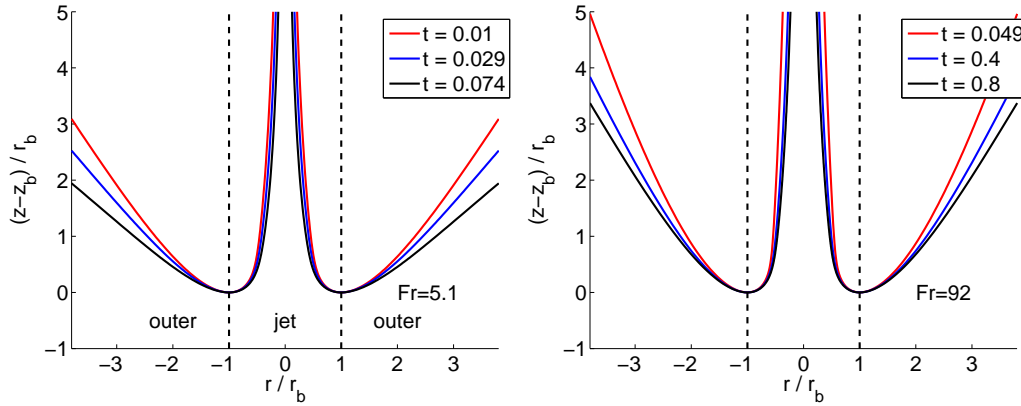


FIGURE 10. Shapes of the jets depicted in figure 9 when distances are normalized using r_b overlay reasonably well indicating that r_b is a good choice for the characteristic local length scale. The definition of the outer and jet regions is also indicated.

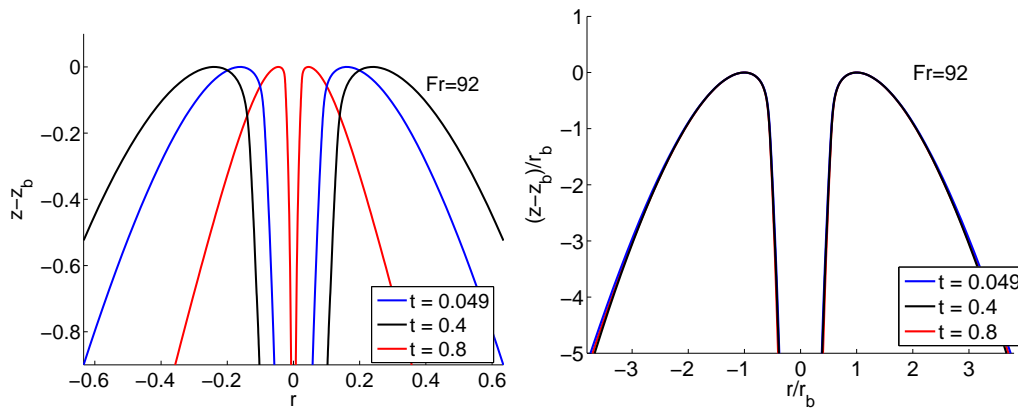


FIGURE 11. Jet shapes for the downward jet at $Fr=92$ taken at the same times as in figures 9 and 10 show a similarly good rescaling with the corresponding base radius r_b .

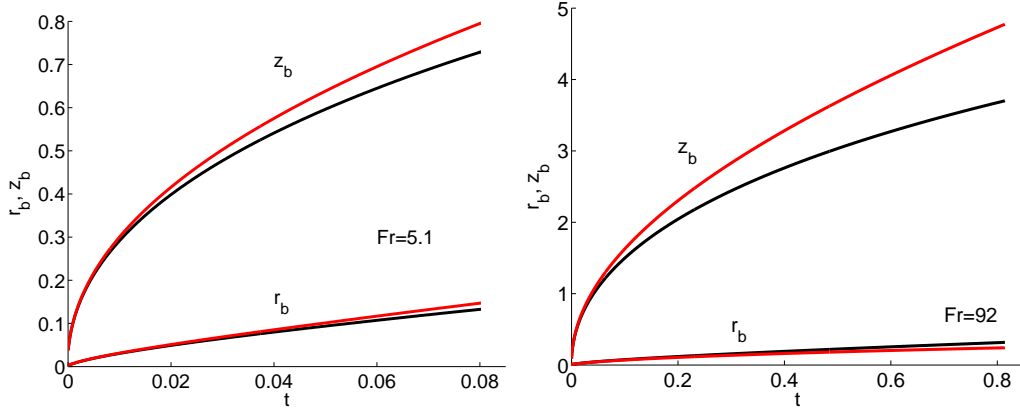


FIGURE 12. Time evolution of radial and axial positions of the jet base, r_b and z_b respectively. The upward jet is shown in black and the downward in red (for the downward jet $-z_b$ is shown for convenience). The behavior of both jets is very similar.

in figure 13 where both the axial and radial velocities evaluated at the jet air/liquid interface, u and v respectively, are represented for different instants of time. In this figure one can observe that while the axial velocities are of similar magnitude as the radial velocities at $r = r_b$, they monotonically increase to much higher values as the jet radius diminishes. Contrarily, the modulus of the (negative) radial velocities decays from $\sim O(10)$ at $r = r_b$ to zero at $r \simeq 0.5r_b$ and, therefore, the radial inflow experiences a strong deceleration in the *small* distance $\sim 0.5r_b$. Since the liquid is at atmospheric pressure at the free surface of the jet, the strong radial deceleration provokes an overpressure below the jet base. Accordingly, a strong favorable *vertical* pressure gradient is created and, therefore, the liquid experiences a large upwards acceleration in the vertical direction, creating the high speed jet ejected into the atmosphere.

In the following, we shall define $r_0 = 0.5r_b$ as the radial position on the jet interface at which radial velocities become negligible $-v \approx 0$ for jet radii smaller than r_0 and the corresponding vertical position and velocity, will be denoted in what follows z_0 and u_0 , respectively. Moreover, we will also define at this point a local Weber number as $We_0 = \rho U_0^2 R_0 / \sigma = We u_0^2 r_0$ whose time evolution is depicted in figure 14. The large values indicate that surface tension effects can be neglected in the description of the jet ejection process.

Thus, since the jet interface can be considered to be at constant atmospheric pressure and surface tension effects are negligible near the jet base, the only source of axial acceleration is the axial pressure gradient caused by the radial deceleration of the flow. Remarkably, this radial deceleration takes place in a very localized region nearby the jet base. (For radial positions on the jet smaller than r_0 already $v \simeq 0$ as shown in figure 13.) Therefore, the source of axial acceleration (radial deceleration) is no longer active high up into the jet, but only near the jet base. This key observation is used to define two of the three different regions within the jet: the *axial acceleration region* for $r_0 < r < r_b$ and $z_b < z < z_0$ and the *ballistic region* for $r < r_0$, $z \geq z_0$. The term used to name the latter region is based on the fact that, since $v \simeq 0$ for $r < r_0$ and the pressure at the jet interface is atmospheric, the momentum equation projected in the axial direction yields

$$\frac{D u}{D t} = 0 \quad \text{for } z > z_0 \quad \text{with } u \neq u(r), \quad (3.1)$$

and D/Dt indicating the material derivative. Equation (3.1) implies that fluid particles

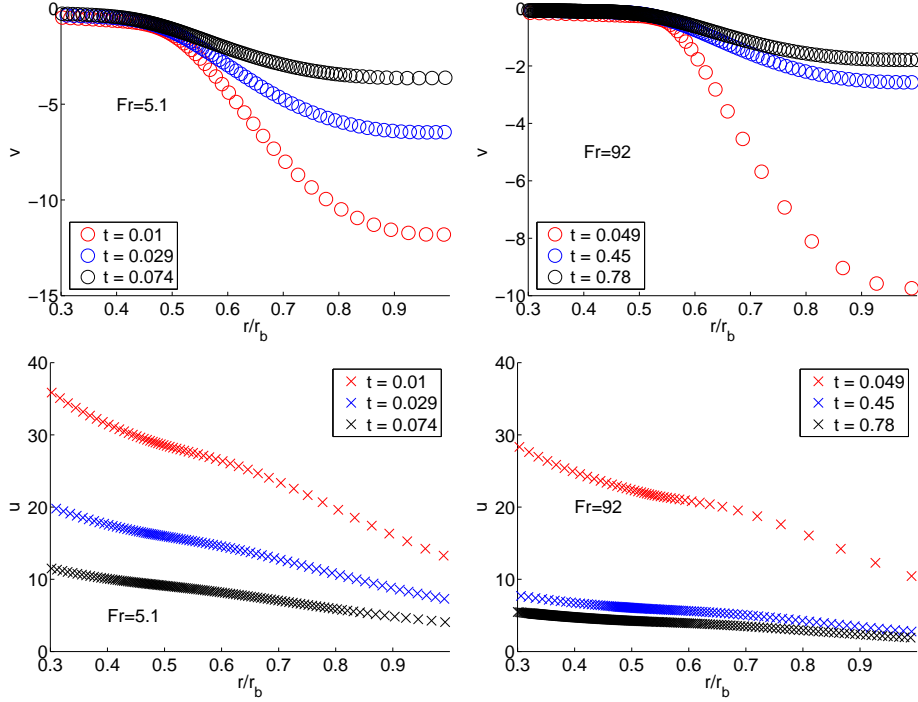


FIGURE 13. Time evolutions of the radial and axial velocities (v and u respectively) of the liquid evaluated at the jet interface for $Fr=5.1$ and $Fr=92$.

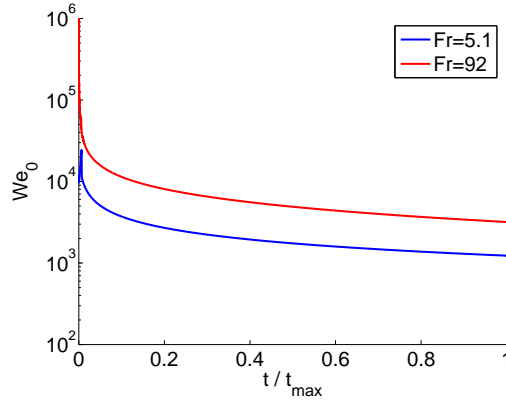
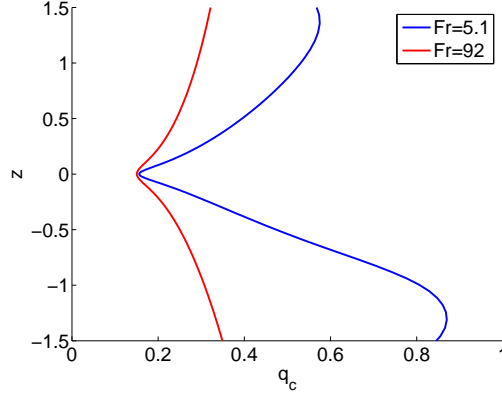
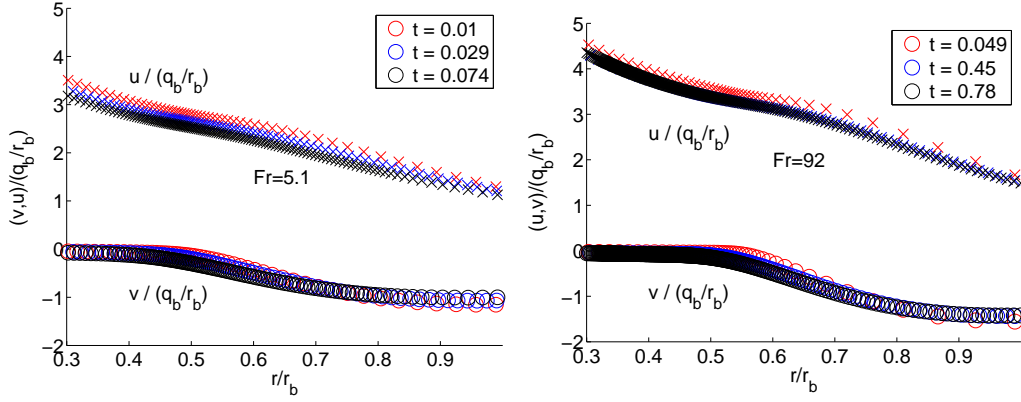


FIGURE 14. Time evolution of the local Weber number at the beginning of the ballistic region for two different values of the impact Froude number. The large values demonstrate that surface tension is not relevant during the jet ejection process. To facilitate the comparison between the different Froude cases, times have been normalized by t_{\max} , which is the time when the downward jet hits the disc and the simulation stops.

are no longer accelerated upwards and conserve the vertical velocities they possess at $z = z_0$, which is the axial boundary between the *axial acceleration region* and the *ballistic region*. In equation (3.1), $u \neq u(r)$ since the radial velocity gradients of axial velocities are negligible in the ballistic region (not shown).

As a next step, we would like to scale the radial velocity field in the vicinity of the jet base which is, as discussed above, the source of momentum driving the jet ejection


 FIGURE 15. The sink strength distribution $q_c(z)$ for two values of the Froude number.

 FIGURE 16. Spatial and temporal evolutions of the radial and axial velocities depicted in figure 13 normalized with $q_b(t)/r_b(t)$. Observe that $u/(q_b/r_b)$ and $v/(q_b/r_b)$ nearly collapse onto the same curves for each of the two values of the impact Froude number considered, $Fr = 5.1$ (a) and $Fr = 92$ (b).

process. These radially inward velocities are originally created by the difference between the hydrostatic pressure in the bulk of the liquid and the gas pressure inside the cavity. After pinch-off however, the radial velocity field feeding the liquid jet is not appreciably modified by gravity during the time evolution of the jet since the local Froude number at the beginning of the ballistic region is $Fr_0 = U_0^2/(gZ_{\text{surface}}) \gg 1$ with Z_{surface} the axial distance between the beginning of the ballistic region and the height of the free surface far from the impact region (see figure 2).

Therefore, the radial velocities which give rise to the jet emergence can be characterized by the sink strength distribution at $t = 0$ right before pinch-off occurs: $q_c(z) = -r_c(z)\dot{r}_c(z)$, where r_c and \dot{r}_c indicate the radius of the cavity and its associated radial velocity, respectively (see Gekle *et al.* (2009a)). The values of $q_c(z)$ are shown in figure 15 for several values of the impact Froude number.

In order to demonstrate the intimate relation of the jet ejection process with the velocity field right before pinch-off, we normalize the velocities v and u at the jet surface (as shown in figure 13) using, as the characteristic scale for velocities, $q_b(t)/r_b(t)$, where $q_b(t) = q_c(z = z_b(t))$ is the sink strength at the height of the jet base. The remarkable result, depicted in figure 16, is that both rescaled velocities nearly collapse onto the same

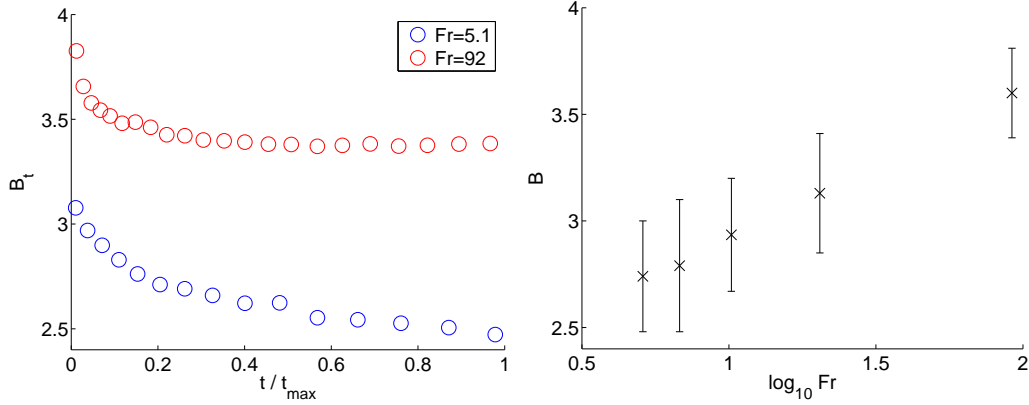


FIGURE 17. (a) The time evolution of B_t demonstrates that B_t is roughly constant in time, but does depend somewhat on the Froude number. (b) Taking the average of B_t over time (with error bars indicating the min/max) for different Froude numbers yields a function $B(Fr)$ which varies only between 2.5 and 3.5 in the range $3 \leq Fr \leq 92$. As indicated in figure 14, t_{\max} is the time when the downward jet hits the disc and the simulation stops.

master curves for a given Froude number and thus are almost constant in time for a fixed value of the rescaled position $r/r_b < 1$. This implies that, for a fixed value of q_b , axial velocities are inversely proportional to r_b i.e., the smaller the jet base radius - or, equivalently, the more confined is the jet by the cavity walls -, the larger will be the axial liquid velocities within the jet.

Of critical importance for our forthcoming discussion is the rescaled axial velocity evaluated at the boundary of the ballistic region, $B_t = u_0(t)/(q_b(t)/r_b(t))$, whose time evolution is depicted in figure 17 (a). In accordance with the collapse of the rescaled velocities on a single master curve depicted in figure 16, B_t hardly changes with time and, thus, we can define the function $B(Fr) = u_0/(q_b/r_b)$ which depends also very weakly on the Froude number, as depicted in figure 17 (b).

The result in figure 17 possesses the additional remarkable implication that axial velocities within the jet are larger than the radial velocities existing at the cavity interface before pinch-off occurs. This can be seen directly by recalling that $|q_b/r_b| = |\dot{r}_b|$, such that B is the ratio between the axial velocity u_0 with which fluid is ejected into the jet and the radial inward velocity at the jet base. Then, during the initial instants of jet formation, $r_b \simeq r_{\min}$, with r_{\min} the minimum radius of the cavity before jet emerges. Therefore, since the maximum radial velocity before pinch-off occurs is $|\dot{r}_{\min}| = |q_c(z=0)/r_{\min}|$, the maximum axial velocity within the jet is given by $\max(u_0) = B(Fr) q_c(z=0)/r_{\min} \sim 3 \dot{r}_{\min}$. This means that, essentially, the velocity with which the jet is ejected is roughly three times larger than the maximum radial velocity attained before pinch-off!

In addition, provided that $We_0 \gg 1$, fluid particles conserve their axial velocity within the ballistic region [see equation (3.1)] and, consequently, the tip of the jet *transports* away from the pinch-off location very valuable information about the largest velocities reached during the cavity collapse process. The knowledge of the function B could thus allow an experimentalist to estimate the maximal pinch-off velocity simply from measurements of the jet tip velocity.

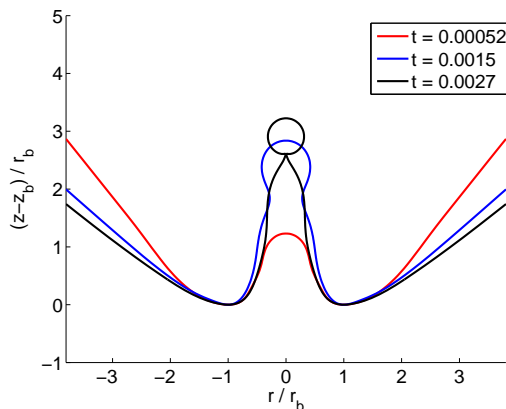


FIGURE 18. The time evolution of the shapes of the jets ejected after bubble pinch-off from an underwater nozzle, show good overlap when distances are normalized using r_b .

3.3. Jet ejection after bubble pinch-off from an underwater nozzle

This section is devoted to the study of Worthington jets which are ejected after the bubble collapse into a liquid pool [Manasseh *et al.* (1998); Bolanos-Jiménez *et al.* (2008)]. As depicted in figure 3, these jets are quite similar to the ones formed after the impact of a solid body against a free surface and, thus, we expect that the conclusions of section 3.2 can be also used for their description.

Figure 18 shows that, similarly to section 3.2, the different shapes nearly collapse onto the same master curve when distances are normalized using r_b . This fact corroborates that r_b is also the correct length scale to characterize this type of jets. However, differently to the case of Worthington jets ejected after the impact of a solid body against a free surface, in which $We_0 \gtrsim 10^3$, the local Weber number evaluated at the beginning of the ballistic region is $\sim O(10)$ in this case (see figure 19a). As a consequence of this, the total length at breakup of these jets is $\sim O(r_b)$ (see figure 18), i.e, much shorter than the length of the Worthington jets in section 3.2. Moreover, such comparatively low values of the local Weber number indicate that surface tension has an effect in the description of the jet ballistic region. This is clearly appreciated in figures 18 and 20 where the collapse onto each other of the normalized time evolutions of the axial and radial velocity components evaluated at the free surface (u and v) is also a bit deteriorated when compared with the case depicted in figure 16. Nevertheless, the two main prerequisites for the model to be presented in the following sections are also satisfied in this case: firstly, the acceleration and ballistic regions are clearly differentiated in figure 20 and, secondly, the normalization of the interfacial velocities with q_b/r_b leads to a reasonable collapse onto a single master curve (see figure 20).

3.4. Jet breakup

The growth of capillary perturbations in a cylindrical liquid jet, firstly quantified by Rayleigh (1878) [see also Eggers & Villermaux (2008)], is based on the assumption that fluid particles conserve, to first order, their longitudinal velocity U . Rayleigh's analysis shows that, moving in a frame of reference with the jet velocity U (which in his case is constant $U \neq U(z, t)$), and no matter how large the Weber number is, the jet breaks due to the growth of capillary perturbations of wavelengths larger than the jet perimeter. The characteristic time needed for such perturbations to disrupt the jet into drops is the capillary time, $\sim (\rho R^3/\sigma)^{1/2}$, with R the jet radius. Therefore the jet breakup length, L_b ,

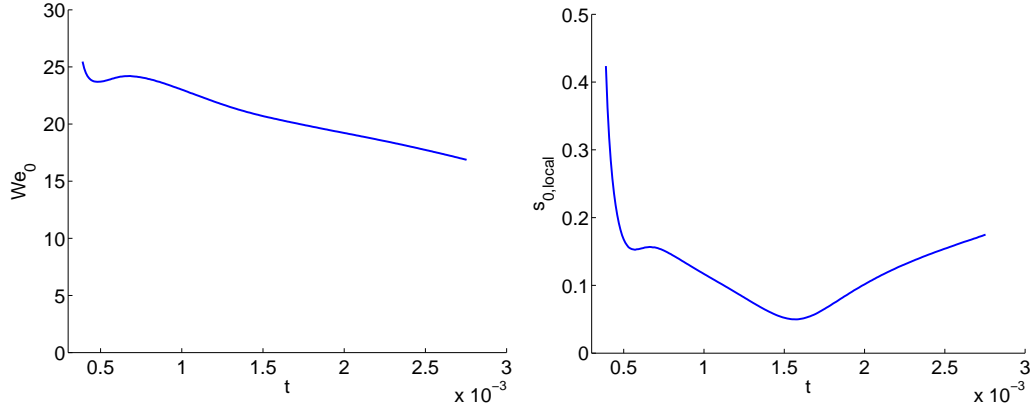


FIGURE 19. (a) Time evolution of the local Weber number for the jet depicted in figure 3. (b) Time evolution of the normalized strain rate $s_{0,local}$ at the beginning of the ballistic region for the same case as in (a).

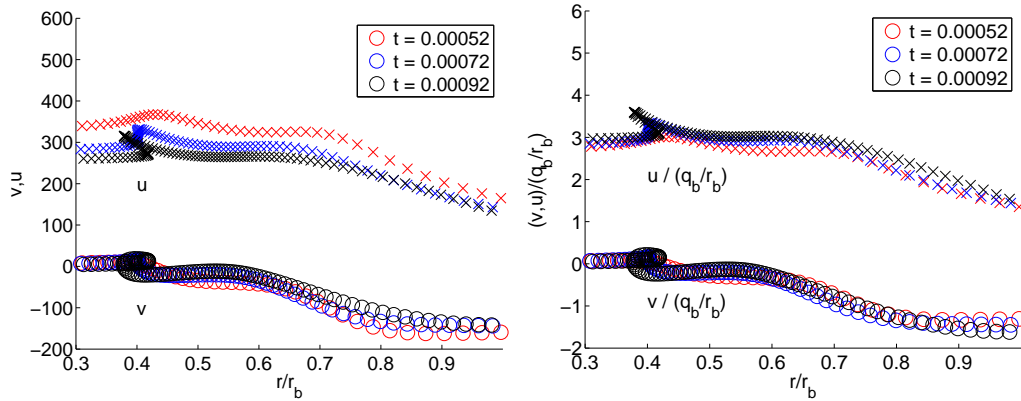


FIGURE 20. (a) Axial and radial velocities evaluated at the jet interface for the case depicted in figure 3. In analogy with figure 16, both the acceleration and ballistic regions are clearly identified: the modulus of the radial velocities decreases from $r = r_b$ to become negligibly small for $r/r_b \lesssim 0.5$. (b) The same as in (a), but with velocities scaled with q_b/r_b . Due to the fact that the Weber number is considerably smaller in this case than for the impacting disc, the jet tip region can be appreciated in this figure as the multivalued part of the curves u and v for $r/r_b \approx 0.4$.

is such that $L_b/R \propto (\rho U^2 R/\sigma)^{1/2}$ if aerodynamic effects are absent [Sterling & Sleicher (1975); Gordillo & Pérez-Saborid (2005)]. Notice that the study of jet breakup in our case is somewhat related to that considered by Rayleigh since the fluid particles conserve their velocities, in a first approach, along the ballistic region of the jet.

Similarly to the case considered by Rayleigh (1878), the study of the capillary breakup of stretched jets will be divided in two: the calculation of the *basic flow*, which is free of capillary effects and the analysis of capillary waves propagating and growing in amplitude at the jet tip region. Viscous effects will be neglected in the analysis.

3.4.1. Unperturbed flow

If $We_0 \gg 1$, the time evolution of both the jet radius and the liquid velocities in the ballistic region can be calculated neglecting surface tension forces and making use of the slenderness of the jet. However, differently to the case considered by Rayleigh (1878), in

which the jet radius $r_j = 1$ and $u = \text{constant}$, here u and r_j are functions of z and t . In effect, if the fluid is assumed to follow a purely vertical motion inside the ballistic region, the couple of equations that determine u and r_j are the momentum equation (3.1), which can be also written as

$$\frac{Du}{Dt} = 0 \rightarrow \frac{\partial u}{\partial t} + u \frac{\partial u}{\partial z} = 0, \quad (3.2)$$

and the unidirectional version of the continuity equation, namely,

$$\frac{\partial r_j^2}{\partial t} + \frac{\partial(u r_j^2)}{\partial z} = 0 \rightarrow \frac{D \ln r_j^2}{Dt} = -\frac{\partial u}{\partial z}, \quad (3.3)$$

where $D/Dt \equiv \partial/\partial t + u\partial/\partial z$ indicates again the material derivative. From equations (3.2)-(3.3), u , r_j and z_j - the height at which the jet radius is r_j - are completely determined if the relevant quantities at the beginning of the ballistic region (r_0 , z_0 , and the velocity u_0) are known functions of time. Indeed, equation (3.2) expresses that fluid particles conserve the vertical velocity they possess at the beginning of the ballistic region. Consequently, a particle ejected from the acceleration into the ballistic region at time $\tau < t$ will, at time t , have attained a height

$$z_j(t) = z_0(\tau) + (t - \tau) u_0(\tau). \quad (3.4)$$

To obtain the corresponding jet radius r_j , equation (3.3) can be readily integrated to give

$$r_j^2(z = z_j, t) = r_o^2(\tau) \frac{u_o(\tau) - dz_o/d\tau}{u_o(\tau) - dz_o/d\tau - du_o(\tau)/d\tau(t - \tau)}. \quad (3.5)$$

Introducing the definition of the strain rate at the beginning of the ballistic region

$$s_o(\tau) = \frac{\partial u}{\partial z}(z = z_0) = -\frac{\dot{u}_o(\tau)}{u_o(\tau) - \dot{z}_o(\tau)} \quad (3.6)$$

allows us to rewrite equation (3.5) in a more compact form as

$$r_j^2(z_j, t) = \frac{r_o^2(\tau)}{1 + (t - \tau)s_o}. \quad (3.7)$$

Note that Rayleigh's original analysis, $u = \text{constant}$ and $r_j = 1$ (cylindrical jet) may be recovered from equations (3.2)-(3.3) by setting $s_0 = 0$ and u_0 , z_0 and r_0 constants in time. However, in our case, $\dot{u}_0 < 0$ and $u_0 = Bq_b/r_b > \dot{z}_b \simeq \dot{z}_0$ and, therefore, by virtue of equation (3.6), these conditions imply $s_o > 0$; consequently, from equation (3.7), the jet is not cylindrical since it stretches downstream.

Now, in order to obtain the complete jet shape at time t , we vary τ between 0 and t and use equations (3.4) and (3.5) to compute the corresponding vertical and radial coordinates of the jet. Note that, clearly, the particle ejected at $\tau = 0$ will end up forming the tip of the jet. The comparison between the numerical results and those obtained from the integration of (3.2)-(3.3), with the values of $u_o(\tau)$, $z_o(\tau)$ and $r_o(\tau)$ taken from the numerical simulations, is depicted in figure 21. The excellent agreement between numerics and the model validates the approach of considering that fluid particles conserve their axial velocities within the ballistic region. It should be pointed out, however, that equations (3.2)-(3.3) need to be corrected at the tip of the jet, where surface tension effects need to be retained.

3.4.2. Growth of capillary disturbances

The linear stability analysis for the type of velocity field given in section 3.4.1 was firstly accomplished by Frankel & Weihs (1985), who recovered Rayleigh's original result

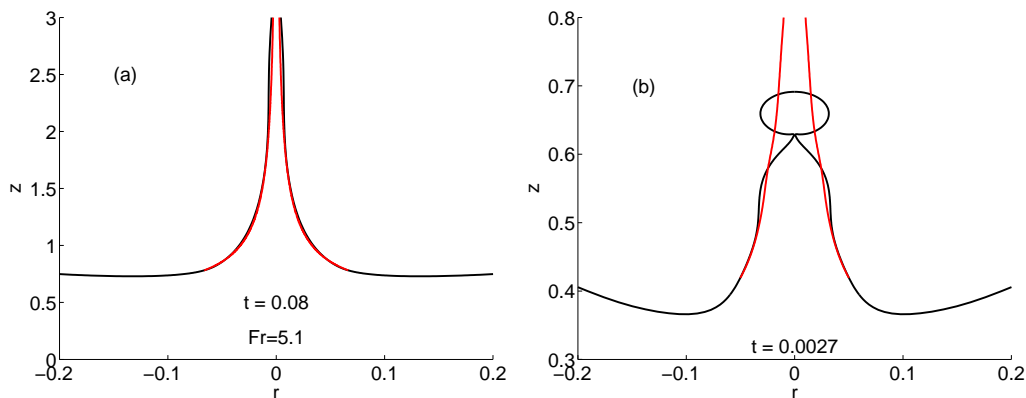


FIGURE 21. Comparison between the numerical jet shape and that obtained from equation (3.5) for the disc impact at $Fr=5.1$ (a) and the jet ejected from the underwater nozzle (b). The black line is the simulation and the red line is the analytical model. The input values of $r_0(t)$, $z_0(t)$ and $u_0(t)$ for the jet stretching model are taken from the simulations. Note that, since surface tension is not included in this model, the tip of the jet requires a separate treatment as described in section 3.4.2

in the limit of $s_0 = 0$. It is our purpose here to extend the analysis on the breakup of stretched jets of Frankel & Weihs (1985) to account for non linear effects and also for the influence of the tip. It is worthy to mention that, in our numerical approach, the wavelength of fastest growth rate is naturally selected by the local flow around the jet tip and, therefore, a linear stability analysis of the type reported in Frankel & Weihs (1985), is avoided.

As a first step, the dimensional counterparts of $r_0(\tau)$ [$R_0(\tau)$] and $u_0(\tau)$ [$U_0(\tau)$] are chosen as the characteristic scales for lengths and velocities, respectively. Consequently, dimensional analysis indicates that the evolution of capillary perturbations in the ballistic region for $t > \tau$ will solely depend on the dimensionless parameters We_0 and $s_{0,local} = S_0(\tau) R_0/U_0 = s_0 r_0/u_0$.

The values of We_0 and $s_{0,local}$ depend non-trivially on the dimensionless parameters controlling the two different physical situations analyzed here. Consequently, in order to study systematically the jet breakup process as a function of $s_{0,local}$ and We_0 we employ the third type of simulations of the axial strain type described in section 2 and illustrated in figure 4. The real jet breakup process can then be reproduced provided that the values of the Weber number and the strain rate at the nozzle exit coincide with those at the beginning of the ballistic region i.e, $We_0 = We_N = \rho U_N^2(0) R_N/\sigma$ and $s_{0,local} = \alpha$.

Note that, since the values of the Weber number based on U_N and ρ_g are always such that $We_g = \rho_g U_N^2 R_N/\sigma \ll 1$, the gas dynamics can be neglected and the only two relevant dimensionless parameters characterizing the axial strain system of figure 4 are We_N and α .

The numerical results depicted in figure 22 show a slender liquid thread which breaks many diameters downstream the nozzle exit. Moreover, it can be observed that the effect of increasing the Weber number is to increase the breakup time and the breakup length. Figure 23 shows a comparison between the shapes of the jets formed after bubble collapse depicted in figure 18 and those obtained from the simulations of the type illustrated in figure 22 with $We_N = We_0(\tau = 0)$ and $\alpha = s_{0,local}(\tau = 0)$. The excellent agreement between both type of numerical results corroborates the fact that tip breakup of Worthington jets can be reproduced by means of the simulations considered in this section

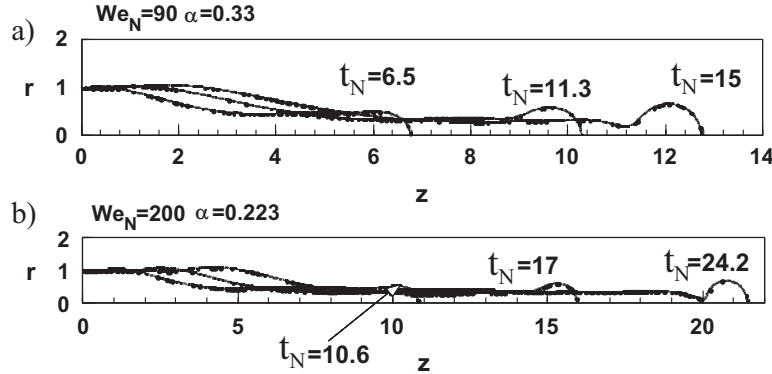


FIGURE 22. Time evolution of jets calculated for two different values of the pair of variables (We_N, α) but the *same* value of the product $We_N \alpha^2$.

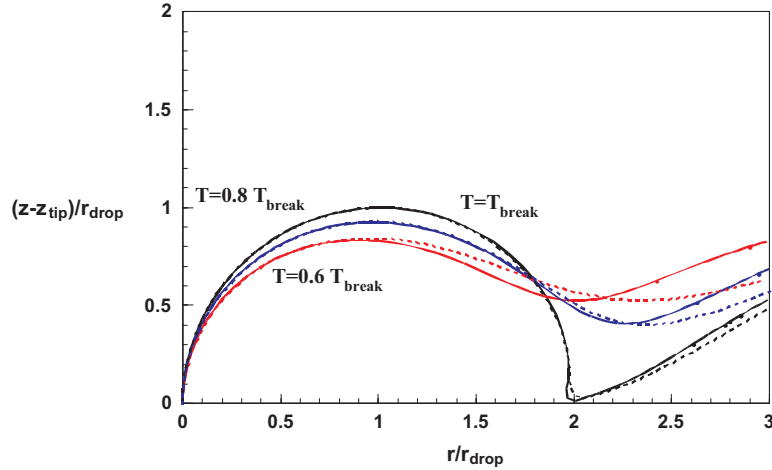


FIGURE 23. Jet shapes of figure 3 (in continuous lines) at three different instants of time ($0.6T_{break}$, $0.8T_{break}$ and T_{break} , with T_{break} the breakup time) compared to those obtained from the type of simulations depicted in figure 22 (dashed lines) for the same values of T . The values of the parameters have been set to $We_N = 25$ and $\alpha = 0.4$ which are the initial values of the local Weber number and the dimensionless axial strain rate of the simulations depicted in figure 19. Note that distances are rescaled using the final radius of the drop R_{drop} as the characteristic length scale and that z_{tip} denotes the axial coordinate of the tip of the jet.

if the values of the parameter We_N and α coincide with the initial values of We_0 and $s_{0,local}$.

However, the numerical code used in this section is unstable for $We_N \gtrsim O(10^3)$. Consequently, the third type of simulations cannot reproduce, at first sight, the breakup of jets ejected by an impacting disc since, in this case, $We_0 \gtrsim 10^3$ as depicted in figure 14. Thus, is it nevertheless possible to describe the breakup process of jets with such high values of We_0 using the numerical simulations of the axial strain type illustrated in figure 4? The answer to this question is affirmative if we realize that, in a frame of reference moving at the tip velocity, the parametrical dependence on the velocity $U_0(\tau = 0)$ disappears. Consequently, since both the local flow field and the jet radius still depends in this frame of reference on $S_0(\tau = 0)$ (see equation (3.6)), dimensional analysis indicates that jet

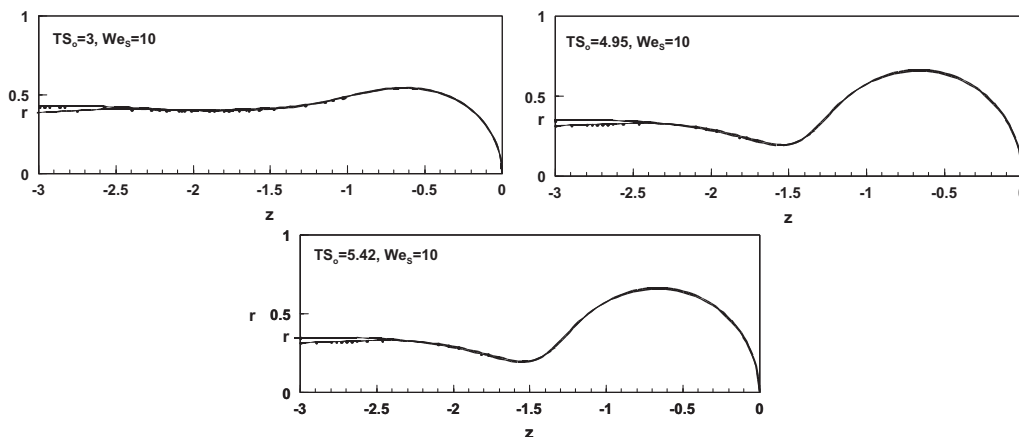


FIGURE 24. Translated jet shapes corresponding to the conditions $We_N = 90$, $\alpha = 0.33$ and $We_N = 200$ and $\alpha = 0.223$, depicted in figures 22 (a) and (b), respectively. Since $We_S = We_N \alpha^2 = 10$ in both cases, the time evolution near the tip region is identical in the normalized temporal variable TS_0 .

breakup can be described in terms of the dimensionless variables TS_0 (or, analogously, $t_N \alpha$) and $We_S = \rho S_0^2 R_0^3 / \sigma = We r_0^3 s_0^2 = We_0 s_{0,local}^2$ (or, analogously, $We_N \alpha^2$).

To check this, the results depicted in figure 22, which correspond to different values of We_N and α but to the same value of $We_N \alpha^2$, are represented in figure 24. Remarkably, the different jet shapes superimpose onto each other for the same values of the dimensionless time TS_0 , what indicates that the breakup process depends solely on We_S (or, equivalently, on $We_N \alpha^2$) and on the dimensionless time TS_0 (or, equivalently, on $t_N \alpha$) for sufficiently large values of We_0 . Figure 25 illustrates that the volume of the nearly spherical drops formed at breakup, decreases for increasing values of We_S . In figure 25 note also that the range of values of We_S investigated is realistic even for the impacting disc, as depicted in 26. Consequently, even though We_0 in some situations such as the disc may be very high, the important parameter which is $We_S = We_0 s_{0,local}^2$ can be matched to the simulations in this section. The dimensionless breakup time and the dimensionless size of the drops in figure 27 behave as $r_{drop} \propto We_S^{-1/7}$ and $(TS_0)_{break} \propto We_S^{2/7}$, respectively. A detailed corresponding theory will be the subject of a forthcoming contribution [Gordillo (2009)]. We emphasize that figure 27 describes a universal relation for the breakup of Worthington jets at high Weber numbers which allows one to obtain the breakup time and volume of the first ejected droplet knowing merely the value of We_S defined at the beginning of jet formation.

Finally, note that, in order for $We_N < O(10^3)$, the computations have been performed choosing $1 \ll We_N \ll We_0$ and, correspondingly, $\alpha > s_{0,local}$. The condition $We_N \gg 1$ is essential since, if We_N was not sufficiently large, the jet breakup process of real Worthington jets would depend on the liquid velocity $U_N(0)$ and, thus, on We_N and α separately.

4. Modeling the jet ejection and breakup processes

Here we aim to develop a model to explain, in simple terms, the jet ejection and breakup processes. Our model will be based on the main conclusions of the previous section which are: (i) both r_b and z_b are *local* quantities which, therefore, do not depend on the large scales of the flow, (ii) the velocity field within the jet can be characterized

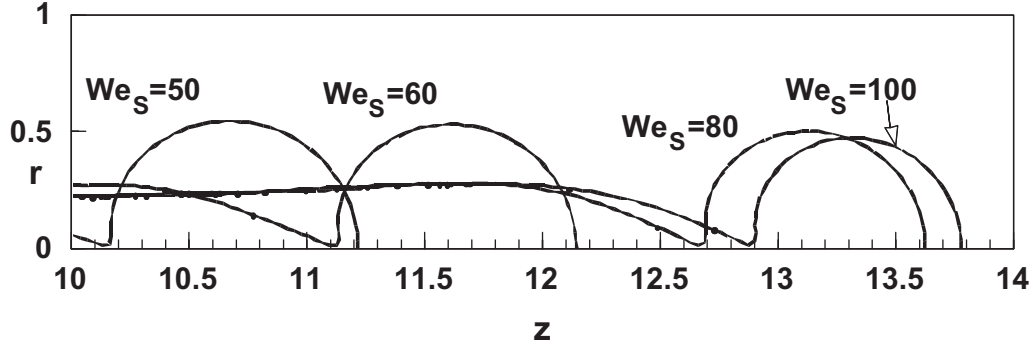


FIGURE 25. Tip region at the instant of breakup for different values of We_S . Observe that the drops generated are nearly spherical and that their volume decreases for increasing values of We_S .

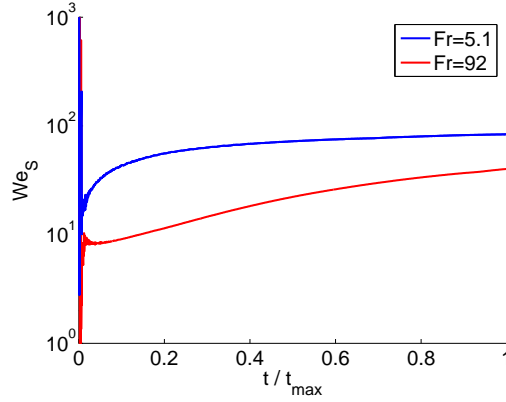


FIGURE 26. Time evolution of the normalized Weber number $We_S = We_0 s_{0,local}^2$ for the impacting disc. As indicated in figure 14, t_{max} is the time when the downward jet hits the disc and the simulation stops.

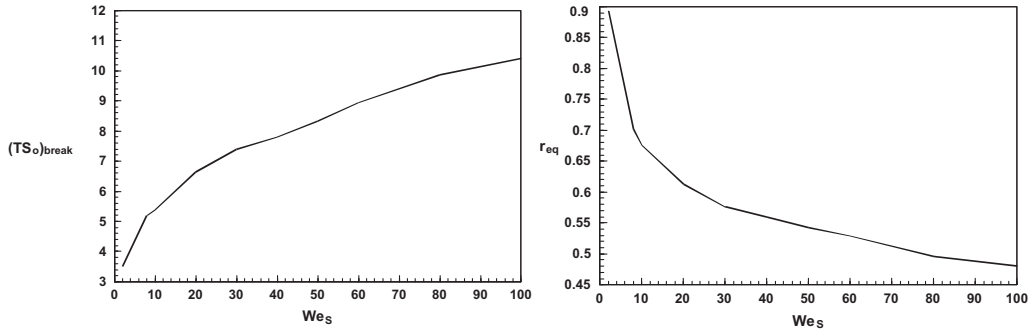


FIGURE 27. Numerical results of the dimensionless breakup time, $(TS_0)_{break}$ (a), and the dimensionless equivalent radius, r_{eq} (b), with $4/3\pi r_{eq}^3 R_0^3$ the volume of the drops formed.

solely in terms of the sink strength intensity at pinch-off, $q_c(z)$ and (iii) the flow field within the jet can be divided in three parts: the *acceleration region*, the *ballistic region* and the *jet tip region*.

This section is structured as follows: in subsection 4.1 $r_b(t)$ and $z_b(t)$ are calculated in

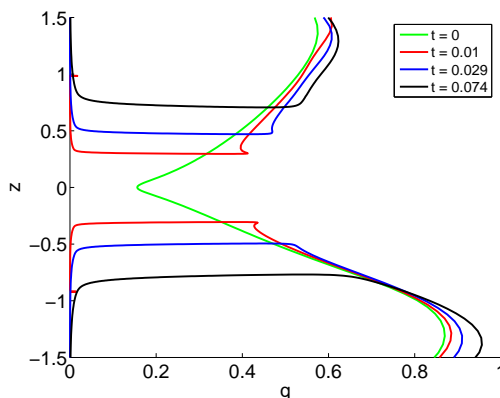


FIGURE 28. The sink distribution $q_c(z)$ at the moment of pinch-off (green) for the impacting disc at $Fr=5.1$ is the essential ingredient to our jet formation model. The sink distributions at later times (red, blue and black curves) are almost unchanged with respect to the sink distribution at pinch-off, confirming our model assumption that $q_c(z)$ is valid even for jet formation when two additional effects are accounted for: the accumulation of sinks around the base and the hole between the up- and the downward jet.

terms of *only* $q_c(z)$ using the theory developed in Gekle *et al.* (2009a). Then, in section 4.2 the axial velocity and the jet shape within the ballistic portion of the jet are calculated through equations (3.2)-(3.3) using, as initial conditions, $r_0 = 0.5 r_b$, $u_0 = B(Fr) q_b/r_b$ and $z_0(\tau) = z_b(\tau) + 0.5r_b$.

4.1. Reviewing the model for $r_b(t)$ and $z_b(t)$

In this subsection we will very briefly review our model for jet formation as presented in Gekle *et al.* (2009a) and show its applications to predict the flow fields as well as the dynamics of the jet base for the impacting disc at $Fr=5.1$ and $Fr=92$ and the Worthington jets created after bubble pinch-off from an underwater nozzle.

The starting point of our model is the description of the cavity collapse using a line of sinks on the axis of symmetry as depicted in figure 15. After pinch-off most of this distribution remains intact with two notable exceptions: a hole is created between the bases of the up- and downward jet and sinks accumulate around the jet base [Gekle *et al.* (2009a)]. These effects are illustrated in figure 28. Based on this observation we derived in Gekle *et al.* (2009a) an analytical expression for the flow potential ϕ at an arbitrary point in the outer region (note that by construction the model is not valid inside the jet itself):

$$2\phi = \underbrace{-q_b \int_{-\infty}^{\infty} \frac{dz'}{\sqrt{r^2 + (z - z')^2}}}_{\text{collapsing cavity}} + \underbrace{q_b \int_{-z_b}^{z_b} \frac{dz'}{\sqrt{r^2 + (z - z')^2}}}_{\text{hole}} + \underbrace{\frac{C q_b r_b}{\sqrt{r^2 + (z - (z_b + C_{\text{sink}} r_b))^2}}}_{\text{point sink}} \quad (4.1)$$

with the order one constants C and C_{sink} chosen appropriately.

As shown in Gekle *et al.* (2009a) this model can be used to predict the temporal evolution of the jet base, i.e. the widening and upwards motion of the jet base. Here we will restrict ourselves to show the result of this procedure for the different systems studied in this work, which are depicted in figure 29.

In fact, as shown in figure 30, equation (4.1) can also be used to predict the entire flow field in the outer region. Figures 29-30 illustrate the rather good agreement between theory and numerics, which we find in all cases studied.

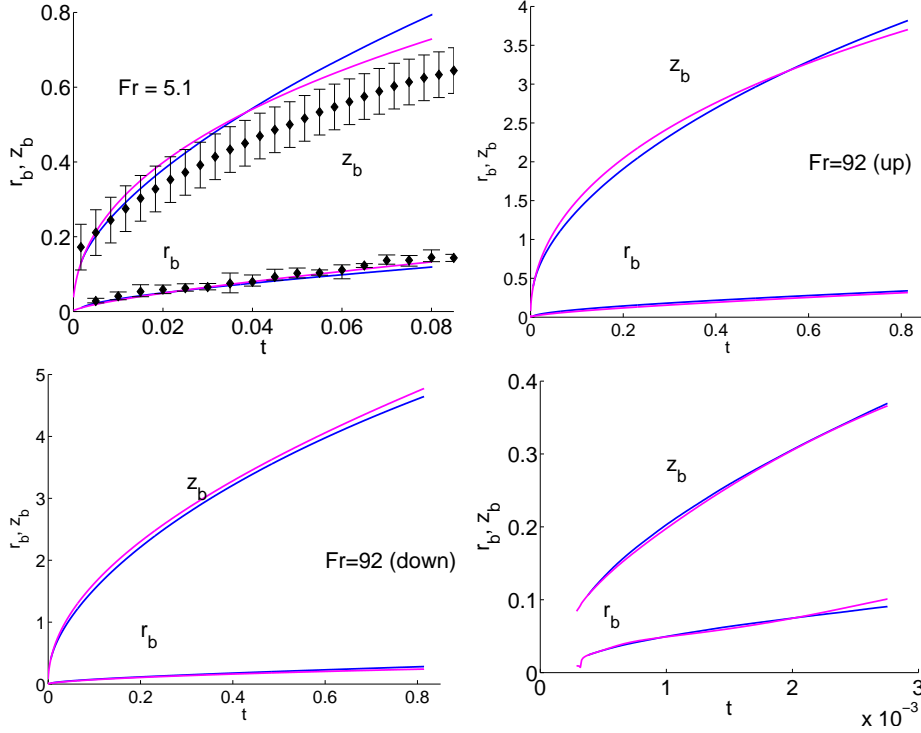


FIGURE 29. Time evolution of the jet base radial and axial positions, r_b and z_b respectively, taken from the simulation (magenta lines) and the analytical model (blue lines). (a) Impacting disc with $Fr=5.1$ for the upward jet (here black diamonds represent experimental data) with $C = 4.55$ and $C_{\text{sink}} = 0.63$. (b) Impacting disc with $Fr=92$ (upward jet) with $C = 7.8$ and $C_{\text{sink}} = 0.63$. (c) Impacting disc with $Fr=92$ (downward jet) with $C = 6.66$ and $C_{\text{sink}} = 0.55$. (d) Upwards jet from the underwater nozzle with $C = 4.9$ and $C_{\text{sink}} = 0.76$.

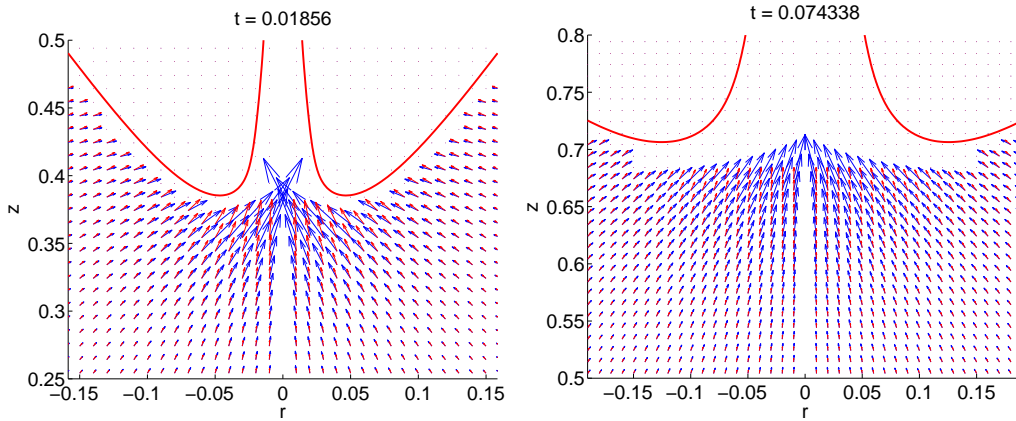


FIGURE 30. The flow field obtained from the model with constants $C = 4.55$ and $C_{\text{sink}} = 0.63$ for the disc impacting at $Fr=5.1$ (blue arrows) shows very good agreement with the numerically calculated flow field (red arrows). The region inside the jet and very close around the base is excluded since the model is not perfectly reliable there (due to the assumption of the observation point far from the base, see Geke *et al.* (2009a)).

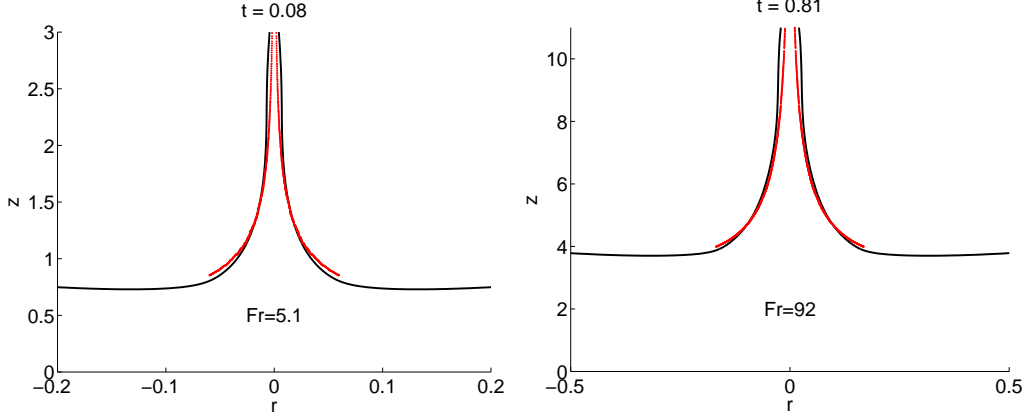


FIGURE 31. Comparison between the jet shape calculated using the boundary integral code (black line) and the one obtained integrating equations (3.2)-(3.3) using the values of r_b and z_b given by the model described in section 4.1 and shown in figure 29 (red line).

4.2. Modeling the jet breakup and drop ejection processes

We will now take the model of the previous section one step further by combining its results with the analysis described in section 3.4.1. This will allow us to predict not only the flow field in the outer region, but also the flow inside the jet and thus the jet shape as a function of time.

Once r_b and z_b are obtained through the model in section 4.1, the axial velocity at the beginning of the ballistic region can be calculated as a function of known quantities as $u_0 \simeq B(\text{Fr})q_b/r_b$, with $B(\text{Fr})$ the function depicted in figure 17. Therefore, both the flow field and the jet shape within the ballistic region can be computed from the integration of equations (3.2)-(3.3) using, as initial conditions, $r_0(\tau) = 0.5 r_b(\tau)$, $u_0(\tau) = B(\text{Fr})q_b(\tau)/r_b(\tau)$ and $z_0(\tau) = z_b(\tau) + 0.5r_b$. The comparison between the jet shape calculated numerically and that obtained from the model is depicted in figure 31 and good agreement is found.

The capillary breakup process of the jet can be also modeled making use of our numerical results in section 3.4.2 since, through equation (3.6), both We_0 and s_0 can be easily expressed as a function of $u_0(\tau) = B q_b/r_b$, $z_b(\tau)$ and $r_b(\tau)$, with the latter two functions given by the model as described above. Consequently, both the ejection and breakup process of the jet can be modeled with the only inputs of $q_c(z)$ and r_{min} , i.e. quantities defined *before* pinch-off.

Moreover, the trajectory of the ejected drops can also be modeled using the results of the previous sections. Indeed, the nearly spherical drops ejected from the tip of the jet follow a ballistic trajectory which can be calculated from Newton's second law as

$$\rho \frac{4\pi R_D^3 r_{eq}^3}{3} \frac{dU_{drop}}{dT} = -\frac{1}{2}\rho_g U_{drop}^2 c_d \pi r_{eq}^2 R_D^2 - \rho \frac{4\pi R_D^3 r_{eq}^3}{3} g \quad (4.2)$$

with U_{drop} and c_d indicating the drop velocity and the drag coefficient, respectively. The drag term needs to be included since the relative variation of the drop velocity associated to aerodynamic effects, $\Delta U_{drop}/U_{drop}$, can be estimated from equation (4.2), yielding

$$\frac{\Delta U_{drop}}{U_{drop}} \sim -\frac{\rho_g U_{drop} c_d \Delta t_{flight}}{\rho R_D} \quad (4.3)$$

with Δt_{flight} the flight time of the drop. Therefore, since $\Delta t_{flight} \sim U_{drop}/g$ and $U_{drop} \simeq$

$U_0 \simeq V_D B(\text{Fr}) q_b/r_b$, the relative variation of drop velocity associated to aerodynamic forces is given by

$$\frac{\Delta U_{drop}}{U_{drop}} \sim -\frac{\rho_g U_{drop}^2}{\rho g R_D} \sim -\frac{\rho_g q_b^2}{\rho r_b^3} \text{Fr} \sim O(1). \quad (4.4)$$

It needs to be pointed out that the validity of equation (4.2) rests on the assumption that drops conserve their spherical shape along their trajectory and, thus, are not atomized due to aerodynamic effects. This will be the case whenever the aerodynamic Weber number $\text{We}_a = \rho_g U_{drop}^2 R_D r_{drop}/\sigma \sim \rho_g/\rho \text{We}_0 \lesssim 6$ [Hanson *et al.* (1963); Villermaux (2007, 2009)]. Therefore, except for the very initial instants after cavity pinch-off, in which the gas Weber number could be larger than 6 - as can be inferred from figure 14 -, equation (4.2) is valid to calculate the drop velocity.

We are now able to calculate the trajectories of the drops ejected from the jet tip. Indeed, once the constants C and C_{sink} of the jet base model in section 4.1 are properly chosen, they determine the values of We_0 and $s_{0,local}$, which are the only inputs for the model and simulations described in section 3.4. With this knowledge, the numerical results of the type illustrated in figures 25 and 27 (which only depend on We_S and TS_0) allow one to calculate the size, velocity and ejection time of the first ejected droplet, the only inputs needed for the integration of equation 4.2.

5. Conclusions

Using detailed boundary-integral simulations together with analytical modeling, we have studied the formation and breakup of the high-speed Worthington jets ejected either after the impact of a solid object on a liquid surface or after the pinch-off of a gas bubble from an underwater nozzle. To describe the phenomenon as a whole we divided the flow structure in two parts separated by the jet base (r_b, z_b): the *outer region* for $r > r_b, z < z_b$ and the jet region, extending from the jet base to the axis i.e. $r < r_b$ and $z \geq z_b$. The jet region is further subdivided into the three subregions: The *axial acceleration region*, where the radial inflow induced by the cavity collapse is decelerated radially and accelerated axially, the *ballistic region*, where fluid particles are no longer accelerated vertically and, thus, conserve the axial momentum they possess at the end of the acceleration region and the *jet tip region*, which is where the jet breakup process occurs.

We first show that the flow in the *outer region* is well described by the analytical model presented in Gekle *et al.* (2009a). This model further provides a set of equations for the time evolution of the jet base $r_b(t)$ and $z_b(t)$. As depicted in figures 29 and 30, the analytical predictions are in remarkable agreement with numerical simulations for the up- and downwards jets of the disc impact as well as the upwards jet created after the bubble pinch-off from an underwater nozzle. The model uses as its only input parameters the minimum radius of the cavity r_{min} and the sink strength $q_c(z)$, both taken at the moment of pinch-off.

The *axial acceleration region*, of characteristic length $O(r_b) \ll z_b$ is where the fluid is decelerated in the radial direction which causes an overpressure that accelerates the fluid vertically. This is thus a very narrow region, localized nearby the jet base, of crucial importance for the jet ejection process since it is where the fluid particles transform their radial momentum into axial momentum. We have found the remarkable result that both radial (v) and axial (u) velocities, when normalized with $q_c(z = z_b)/r_b = q_b/r_b$, nearly collapse onto the same master curves for both the disc and the nozzle. Therefore, the values of the rescaled velocities $(u, v)/(q_b/r_b)$ are almost constant in time for a fixed value of the rescaled position $r/r_b < 1$. We have also found that $v/(q_b/r_b) \simeq 0$ for

that part of jet surface whose radius is smaller than $r_0 = 0.5 r_b$. Therefore, since the source of axial acceleration - radial deceleration of the fluid - is no longer active when $r < r_0$ the corresponding vertical position z_0 constitutes the upper boundary of the acceleration region. In addition, we have found that the normalized axial velocity at z_0 , $u_0/(q_b/r_b) = B$ is a function which depends very weakly on time and on the Froude number for the impacting disc case (see figure 17).

In the slender *ballistic region* the axial pressure gradients are negligible since $v \simeq 0$ and the Weber number evaluated at the beginning of the ballistic region ($We_0 = We u_0^2 r_0$) is much larger than unity. Therefore, we have developed a 1D model assuming that, in a first approach, fluid particles conserve their vertical velocities along the ballistic portion of the jet. This model allows us to calculate both the velocity field and the jet shape from equations (3.2)-(3.7). The only input parameters are the radius, vertical position, and axial velocity at the beginning of the ballistic region. For the impacting disc, these values $r_0(t)$, $z_0(t)$, and $u_0(t)$, respectively, can be obtained directly from the analytical model of the outer region together with the function $B(Fr) \simeq \text{constant}$ describing the acceleration region. For the underwater nozzle, the input parameters are provided directly by the numerical simulation. The results of this new model for the jet shape are in remarkable agreement with numerical simulations, as depicted in figures 21 and 31.

Finally, we have analyzed the *tip break-up region* of the stretched jet. The main result is that the jet capillary breakup can be described as a function of two dimensionless parameters: the local Weber number We_0 and the strain rate evaluated at the beginning of the ballistic region, $s_0 = \partial u / \partial z (z = z_0)$. Both quantities can again be obtained either from the numerical simulations or from the models of the outer and acceleration regions. In order to study systematically the jet breakup process as a function of these two values we have simulated the injection of a liquid into the atmosphere from a nozzle of constant radius (see figure 4). The real jet breakup process can then be reproduced provided that the values of the Weber number and the strain rate at the nozzle exit coincide with those at the beginning of the ballistic region, as shown in figure 23.

We have found that the tip breakup in our physical situations is not triggered by the growth of perturbations coming from an external source of noise. Instead, the jet breaks up due to the capillary deceleration of the liquid at the tip, which produces a corrugation to the jet shape. Moreover, for sufficiently large values of We_0 , the time evolution of the tip of the jet does not depend on We_0 and s_0 separately, but can be described in terms of the dimensionless parameter $We_S = We r_0^3 s_0^2$ and the rescaled time TS_0 . This universal description allows us thus to obtain the size of the droplet ejected from the tip (cf. figure 27) if We_0 and s_0 are known from either simulations, measurements, or analytical models such as the one described in Gekle *et al.* (2009a).

In summary, our description of Worthington jets created by the impact of a solid object on a liquid surface allows us to predict the jet base dynamics, the jet shape, and even the ejection of drops from the tip of the jet based *only* on the knowledge of the minimum radius of the cavity before the jet emerges and the sink distribution at pinch-off.

We gratefully acknowledge many helpful discussions with Devaraj van der Meer and Detlef Lohse. We further thank Johanna Bos for providing the experimental data for the jet base, Arjan van der Bos for the photograph in figure 1 and Francisco del Campo-Cortés for the photographs in figures 5-6. JMG thanks financial support by the Spanish Ministry of Education under Project DPI2008-06624- C03-01. SG's contribution is part of the program of the Stichting FOM, which is financially supported by NWO.

REFERENCES

- ANTKOWIAK, A., BREMOND, N., DIZÈS, S. LE & VILLERMAUX, E. 2007 Short-term dynamics of a density interface following an impact. *J. Fluid Mech.* **577**, 241–250.
- BARTOLO, D., JOSSERAND, C. & BONN, D. 2006 Singular jets and bubbles in drop impact. *Phys. Rev. Lett.* **96**, 124501.
- BERGMANN, R., VAN DER MEER, D., GEKLE, S., VAN DER BOS, A. & LOHSE, D. 2009 Controlled impact of a disc on a water surface: Cavity dynamics. *accepted* .
- BERGMANN, R., VAN DER MEER, D., STIJNMAN, M., SANDTKE, M., PROSPERETTI, A. & LOHSE, D. 2006 Giant bubble pinch-off. *Phys. Rev. Lett.* **96**, 154505.
- BIRKHOFF, G. D., MACDONALD, D. P., PUGH, W. M. & TAYLOR, G. I. 1948 Explosives with lined cavities. *J. Appl. Phys.* **19**, 563–582.
- BLAKE, J. R., ROBINSON, P. B., SHIMA, A. & TOMITA, Y. 1993 Interaction of two cavitation bubbles with a rigid boundary. *J. Fluid Mech.* **255**, 707–721.
- BOLANOS-JIMÉNEZ, R., SEVILLA, A., MARTÍNEZ-BAZÁN, C. & GORDILLO, J. M. 2008 Axisymmetric bubble collapse in a quiescent liquid pool. Part II: Experimental study. *Phys. Fluids* **20**, 112104.
- BOLANOS-JIMÉNEZ, R., SEVILLA, A., MARTÍNEZ-BAZÁN, C., VAN DER MEER, D. & GORDILLO, J. M. 2009 The effect of liquid viscosity on bubble pinch-off. *Phys. Fluids* **21**, 072103.
- BOULTON-STONE, J. M. & BLAKE, J. R. 1993 Gas bubbles bursting at a free surface. *J. Fluid Mech.* **254**, 437–466.
- BURTON, J., WALDREP, R. & TABOREK, P. 2005 Scaling instabilities in bubble pinch-off. *Phys. Rev. Lett.* **94**, 184502.
- BURTON, J. C. & TABOREK, P. 2008 Bifurcation from bubble to droplet in inviscid pinch-off. *Phys. Rev. Lett.* **101**, 214502.
- DENG, Q., ANILKUMAR, A. V. & WANG, T. G. 2007 The role of viscosity and surface tension in bubble entrapment during drop impact onto a deep liquid pool. *J. Fluid Mech.* **578**, 119–138.
- DUCHEMIN, L., POPINET, S., JOSSERAND, C. & ZALESKI, S. 2002 Jet formation in bubbles bursting at a free surface. *Phys. Fluids* **14**, 3000–3008.
- DUCLAUX, V., CAILLÉ, F., DUEZ, C., YBERT, C., BOCQUET, L. & CLANET, C. 2007 Dynamics of transient cavities. *J. Fluid Mech.* **591**, 1–19.
- DUEZ, C., YBERT, C., CLANET, C. & BOCQUET, L. 2007 Making a splash with water repellency. *Nat. Phys.* **3**, 180–183.
- EGGERS, J. & VILLERMAUX, E. 2008 Physics of liquid jets. *Rep. Prog. Phys.* **71**, 036601.
- FRANKEL, I. & WEIHS, D. 1985 Stability of a capillary jet with linearly increasing axial velocity (with application to shaped charges). *J. Fluid Mech.* **155**, 289–307.
- GEKLE, S., VAN DER BOS, A., BERGMANN, R., VAN DER MEER, D. & LOHSE, D. 2008 Non-continuous froude number scaling for the closure depth of a cylindrical cavity. *Phys. Rev. Lett.* **100**, 084502.
- GEKLE, S., GORDILLO, J. M., VAN DER MEER, D. & LOHSE, D. 2009a High-speed jet formation after solid object impact. *Phys. Rev. Lett.* **102**, 034502.
- GEKLE, S., PETERS, I., GORDILLO, J. M., VAN DER MEER, D. & LOHSE, D. 2009b Supersonic air flow due to solid-liquid impact. *preprint* .
- GEKLE, S., SNOELJER, J. H., LOHSE, D. & VAN DER MEER, D. 2009c Approach to universality in axisymmetric bubble pinch-off. *preprint* .
- GLASHEEN, J. W. & MCMAHON, T. A. 1996 Vertical water entry of disks at low froude numbers. *Phys. Fluids* **8**, 2078–2083.
- GORDILLO, J. M. 2008 Axisymmetric bubble collapse in a quiescent liquid pool. i. theory and numerical simulations. *Phys. Fluids* **20**, 112103.
- GORDILLO, J. M. 2009 Capillary breakup of stretched liquid jets. *in preparation* .
- GORDILLO, J. M. & PÉREZ-SABORID, M. 2005 Aerodynamic effects in the break-up of liquid jets: on the first wind-induced break-up regime. *J. Fluid Mech.* **541**, 1–20.
- GORDILLO, J. M., SEVILLA, A. & MARTÍNEZ-BAZÁN, C. 2007 Bubbling in a co-flow at high reynolds numbers. *Phys. Fluids* **19**, 077102.
- GORDILLO, J. M., SEVILLA, A., RODRÍGUEZ-RODRÍGUEZ, J. & MARTÍNEZ-BAZÁN, C. 2005 Axisymmetric bubble pinch-off at high reynolds numbers. *Phys. Rev. Lett.* **95**, 194501.

- HANSON, A. R., DOMICH, E. G. & ADAMS, H. S. 1963 Shock tube investigation of the break-up of drops by air blasts. *Phys. Fluids* **6**(8), 1070–1080.
- HOGREFE, J. E., PEFFLEY, N. L., GOODRIDGE, C. L., SHI, W. T., HENTSCHEL, H. G. E. & LATHROP, D. P. 1998 Power-law singularities in gravity-capillary waves. *Physica D* **123**, 183–205.
- KEIM, N. C., MOLLER, P., ZHANG, W. W. & NAGEL, S. R. 2006 Breakup of air bubbles in water: Memory and breakdown of cylindrical symmetry. *Phys. Rev. Lett.* **97**, 144503.
- LEPPINEN, D & LISTER, J R 2003 Capillary pinch-off in inviscid fluids **15**, 568–578.
- LIGER-BELAIR, G., POLIDORI, G. & JEANDET, P. 2008 Recent advances in the science of champagne bubbles. *Chem. Soc. Rev.* **37**, 2490.
- LOHSE, D., BERGMANN, R., MIKKELSEN, R., ZEILSTRA, C., VAN DER MEER, D., VERSLUIS, M., VAN DER WEELE, K., VAN DER HOEF, M. & KUIPERS, H. 2004 Impact on soft sand: void collapse and jet formation. *Phys. Rev. Lett.* **93**, 198003.
- LONGUET-HIGGINS, M. S. 1983 Bubbles, breaking waves and hyperbolic jets at a free surface. *J. Fluid Mech.* **127**, 103–121.
- LONGUET-HIGGINS, M. S., KERMAN, B. R. & LUNDE, K. 1991 The release of air bubbles from an underwater nozzle. *J. Fluid Mech.* **230**, 365–390.
- LONGUET-HIGGINS, M. S. & OGUZ, H. 1995 Critical microjets in collapsing cavities. *J. Fluid Mech.* **290**, 183–201.
- MACINTYRE, F. 1968 Bubbles: A boundary-layer "microtome" for micron-thick samples of a liquid surface. *J. Phys. Chem.* **72**, 589–592.
- MANASSEH, R., YOSHIDA, S. & RUDMAN, M. 1998 Bubble formation processes and bubble acoustic signals. *Third International Conference on Multiphase Flow, ICMF'98 Lyon, France* pp. 1–8.
- MORTON, D., RUDMAN, M. & LIOW, J. L. 2000 An investigation of the flow regimes resulting from splashing drops. *Phys. Fluids* **12**, 747–763.
- OGUZ, H. N. & PROSPERETTI, A. 1990 Bubble entrainment by the impact of drops on liquid surfaces. *J. Fluid Mech.* **219**, 143–179.
- OGUZ, H. N. & PROSPERETTI, A. 1993 Dynamics of bubble growth and detachment from a needle. *J. Fluid Mech.* **257**, 111–145.
- OHL, C. D. & IKINK, R. 2003 Shock-wave-induced jetting of micron-sized bubbles. *Phys. Rev. Lett.* **90**, 214502.
- RAYLEIGH, W. S. 1878 On the instability of jets. *Proc. of the London Math. Soc.* **10**, 4–13.
- REIN, M. 1993 Phenomena of liquid drop impact on solid and liquid surfaces. *Fluid. Dyn. Res.* **12**, 61–93.
- SCHMIDT, L. E., KEIM, N. C., ZHANG, W. W. & NAGEL, S. R. 2009 Memory-encoding vibrations in a disconnecting air bubble. *Nature physics* **5**, 343–346.
- SHIN, J. & MCMAHON, T. A. 1990 The tuning of a splash. *Phys. Fluids A* **2**, 1312–1317.
- STERLING, A.M. & SLEICHER, C.A 1975 The instability of capillary jets. *J. Fluid Mech.* **68**, 477–495.
- THORODDSEN, S.T., ETOH, T.G. & TAKEHARA, K. 2007a Experiments on bubble pinch-off. *Phys. Fluids* **19**, 042101.
- THORODDSEN, S.T., ETOH, T.G. & TAKEHARA, K. 2008 High-speed imaging of drops and bubbles. *Annu. Rev. Fluid Mech.* **40**, 257–285.
- THORODDSEN, S. T., ETOH, T. G. & TAKEHARA, K. 2007b Microjetting from wave focussing on oscillating drops. *Phys. Fluids* **19**, 052101.
- THORODDSEN, S. T. & SHEN, A. Q. 2001 Granular jets. *Phys. Fluids* **13**, 4–6.
- TJAN, K. K. & PHILLIPS, W. R. C. 2007 On impulsively generated inviscid axisymmetric surface jets, waves and drops. *J. Fluid Mech.* **576**, 377–403.
- VILLERMAUX, E. 2007 Fragmentation. *Annu. Rev. Fluid Mech.* **49**, 419–446.
- VILLERMAUX, E. 2009 Single-drop fragmentation determines size distribution of raindrops. *Nat. Phys.* p. DOI: 10.1038/NPHYS1340.
- WORTHINGTON, A. M. & COLE, R. S. 1897 Impact with a liquid surface studied by the aid of instantaneous photography. *Phil. Trans. Royal Soc. Series A* **189**, 137–148.
- WORTHINGTON, A. M. & COLE, R. S. 1900 Impact with a liquid surface studied by the aid of instantaneous photography. paper ii. *Phil. Trans. Royal Soc. Series A* **194**, 175–199.

ZEFF, B. W., KLEBER, B., FINEBERG, J. & LATHROP, D. P. 2000 Singularity dynamics in curvature collapse and jet eruption on a fluid surface. *Nature* **403**, 401–404.